Monthly Notices of the ROYAL ASTRONOMICAL SOCIETY

MNRAS **551**, 1–26 (2026) https://doi.org/10.1093/mnras/stag1369
Advance Access publication 2026 July 20

GA-NIFS: dissecting the alchemised: *JWST* reveals turbulent metal-poor gas fuelling a cospatial starburst in a complex system at $z = 10.17$

Robert G. Pascalau [1,2★], Francesco D'Eugenio [1,2], Roberto Maiolino [1,2,3], Qiao Duan [1,2], Yuki Isobe [1,2,4], Santiago Arribas [5], Andrew J. Bunker [6], Stéphane Charlot [7], Michele Perna [5], Bruno Rodríguez Del Pino [5], Hannah Übler [8], Elena Bertola [9], Torsten Böker [10], Stefano Carniani [11], Dan Coe [10,12,13], Giovanni Cresci [9], Mirko Curti [14], Tiger Y.Y. Hsiao [15], Lucy R. Ivey [1,2], Gareth C. Jones [1,2], Isabella Lamperti [9,16], Eleonora Parlanti [11], Jan Scholtz [1,2], Sandro Tacchella [1,2], Lorenzo Ulivi [5], Giacomo Venturi [11], Joris Witstok [17,18] and Sandra Zamora [11]

Affiliations are listed at the end of the paper

Accepted 2026 July 17. Received 2026 July 8; in original form 2026 February 27

ABSTRACT

Recent observations revealed that distant galaxies have bursty star formation histories, regulated by stellar or active galactic nuclei (AGNs) feedback and gas inflows. According to theoretical models, feedback preferentially removes metal-rich gas, while subsequent starbursts are triggered by mergers and newly accreted gas that is generally less enriched than the galaxy's interstellar medium (ISM). Therefore, gas-phase metallicity provides key insights into the baryonic processes shaping early galaxies. We present the first NIRSpec/integral-field unit (IFU) study of spatially resolved ISM properties in the MACS0647-JD system ($z = 10.17$). The system consists of two stellar components detected in NIRSpec/IFU (Near-InfraRed Spectrograph Integral Field Unit) and NIRCam (Near-InfraRed Camera) photometry. The main component ($\log(M_*/\mathrm{M}_\odot) = 7.77 \pm 0.09$; $12 + \log(\mathrm{O/H}) = 7.89 \pm 0.16$) is more massive and significantly more metal-rich compared to its companion ($\log(M_*/\mathrm{M}_\odot) = 7.42 \pm 0.07$; $12 + \log(\mathrm{O/H}) = 7.47 \pm 0.20$), suggesting an older stellar population and a prolonged chemical enrichment history. We find that the Hγ line emission centroid is spatially offset by ~ 0.1 arcsec (150 pc in the source plane) from the stellar continuum centroid; the latter coincides with the location of the main stellar component. This offset provides possible evidence of a merger-driven starburst in this system. By comparing the spatial distributions of the metallicity, velocity dispersion, and the burstiness of star formation history, we infer the presence of turbulent, metal-poor gas outside the stellar components. This metal-poor, dynamically unstable gas is likely responsible for the enhanced recent star formation in the north-east region of the system.

Key words: ISM: kinematics and dynamics – galaxies: abundances – galaxies: evolution – galaxies: high-redshift – galaxies: ISM.

1 INTRODUCTION

Theoretical models posit that early galaxies had variable star formation histories (SFHs), characterized by multiple episodes of intense star formation, each followed by periods of lower activity (X. Ma et al. 2018; C.-A. Faucher-Giguère 2018; K. G. Iyer et al. 2020; S. Tacchella, J. C. Forbes & N. Caplar 2020; T. Dome et al. 2024; W. McClymont et al. 2025). *James Webb Space Telescope* (*JWST*) observations are confirming this picture, with the discovery of a plethora of galaxies in each of these phases: starbursts (K. Boyett et al. 2024; A. Dressler et al. 2024; D. Langeroodi & J. Hjorth 2024; R. Endsley et al. 2025; T. J. Looser et al. 2025; C. Witten et al. 2025) and quenched (V. Strait et al. 2023; T. J. Looser et al. 2024; W. M. Baker et al. 2025; A. Covelo-Paz et al. 2026). One of the key tracers of SFHs is gas-phase metallicity, which carries the imprint of a number of mechanisms shaping the evolution of galaxies before Cosmic Noon (R. Davé, K. Finlator & B. D. Oppenheimer 2011; S. J. Lilly et al. 2013; R. S. Somerville & R. Davé 2015; C. Péroux & J. C. Howk 2020). SFHs are regulated by a combination of baryonic processes, including mergers, cosmological gas accretion, and gas outflows driven by stellar (W. M. Baker et al. 2023; S. Zamora et al. 2025a) or active galactic nuclei (AGNs) feedback (A. C. Fabian 2012; R. Weinberger et al. 2017; M. A. Bourne & H.-Y. K. Yang 2023). Such outflows can efficiently remove metal-enriched gas and suppress star formation, leading

★ E-mail: rgp34@cam.ac.uk

to quiescent phases (A. C. Fabian 2012; P. F. Hopkins et al. 2014, 2023). Conversely, mergers and metal-poor inflows of dense gas can rejuvenate galaxies by triggering intense episodes of star formation (D. Kereš et al. 2005; A. Dekel et al. 2009; J. Schaye et al. 2010; M. Sparre et al. 2017; G. Sun et al. 2023; D. Langeroodi & J. Hjorth 2023; C. A. Mason, M. Trenti & T. Treu 2023; H. Yajima et al. 2023).

It has been suggested that gas accretion and bursty star formation lead to increased scatter of the mass–metallicity relation (J. Lequeux et al. 1979; C. A. Tremonti et al. 2004; L. J. Kewley & S. L. Ellison 2008; R. Maiolino et al. 2008; S. F. Sánchez et al. 2017), as reported by simulations (M. E. De Rossi et al. 2017; O. Agertz et al. 2020; A. M. Garcia et al. 2024) and semi-analytical models (e.g. G. De Lucia et al. 2020). Furthermore, simulations reveal a link between stellar feedback and the spatial distribution of metals: models with enhanced stellar feedback lead to efficient mixing of metals in the interstellar medium (ISM), resulting in flatter radial metallicity gradients on average in these cases (B. K. Gibson et al. 2013; A. Mott, E. Spitoni & F. Matteucci 2013; X. Sun et al. 2025; A. M. Garcia et al. 2026). However, such metallicity gradients are physically stable only if these systems had evolved long enough to reach a nearly steady state. Observational evidence for correlations between very recent star formation activity and metallicity on spatially resolved scales in the early Universe remains scarce (e.g. C. Marconcini et al. 2024).

Following the launch of the *JWST* (J. P. Gardner et al. 2023; J. Rigby et al. 2023), it became possible to study rest-frame optical and near-infrared spectra and photometry of distant galaxies less than 1 Gyr after the big bang (A. J. Bunker et al. 2023, 2024; E. Curtis-Lake et al. 2023; S. Fujimoto et al. 2023, 2024; D. Kashino et al. 2023; P. A. Oesch et al. 2023; G. Roberts-Borsani et al. 2023; B. E. Robertson et al. 2023; B. Wang et al. 2023b; F. D'Eugenio et al. 2024b, 2025b; K. N. Hainline et al. 2024; Y. Harikane et al. 2024; C. T. Donnan et al. 2025; C. Marconcini et al. 2025; L. Napolitano et al. 2025; S. H. Price et al. 2025), even up to $z > 14$ (< 300 Myr after the big bang; S. Carniani et al. 2024; R. P. Naidu et al. 2026). In order to understand how galaxies evolve across cosmic time, it is necessary to constrain the properties of their ISM.

Owing to its unprecedented near-infrared sensitivity, and its ability to provide high spatial resolution (sub-kpc scales) and $R \sim 1000 - 3000$ spectra unaffected by telluric lines and atmospheric effects, *JWST*/NIRSpec (P. Jakobsen et al. 2022) has completely revolutionized our understanding of galaxy formation and evolution before Cosmic Noon. These early galaxies have truly extreme ISM conditions, including hard radiation fields, high ionization parameters (A. J. Cameron et al. 2023; S. Mascia et al. 2023; R. L. Sanders et al. 2023b; M. Tang et al. 2023; K. Boyett et al. 2024; A. Calabrò et al. 2024; M. W. Topping et al. 2024, 2025b), high electron number densities (Y. Isobe et al. 2023b; N. A. Reddy et al. 2023; J. Li et al. 2025; M. W. Topping et al. 2025a), and higher electron temperatures combined with lower metallicities compared to lower-z galaxies of similar M_* and star formation rates (SFRs; D. Langeroodi et al. 2023; J. R. Trump et al. 2023; M. Curti et al. 2024; I. H. Laseter et al. 2024; C. L. Pollock et al. 2026). All these observational results are in agreement with the findings of theoretical hydrodynamical simulations such as MEGATRON (N. Choustikov et al. 2026). Moreover, *JWST* observations have substantially increased the number of detections of auroral lines at $2 < z < 10$ (K. Nakajima et al. 2023; I. H. Laseter et al. 2024; T. Morishita et al. 2024; R. L. Sanders et al. 2024; D. Scholte et al. 2025; A. E. Shapley et al. 2025; M. Stiavelli et al. 2025), allowing for accurate calculations of gas-phase metallicities based on the direct-T_e method (M. Peimbert 1967; D. E. Osterbrock 1989). Capitalizing on the capabilities of the NIRSpec integral-field unit (IFU) mode (T. Böker et al. 2022) to reveal spatial and spectral information, a number of recent studies have focused on spatially resolved gas-phase metallicity and ISM properties in galaxies at $z = 2 - 8$. One key strength of IFU studies is their ability to provide in-depth analyses of systems with complex morphologies and intricate kinematics (B. Rodríguez Del Pino et al. 2024; G. C. Jones et al. 2024, 2025b, 2026b; H. Übler et al. 2024; M. A. Marshall et al. 2025a; E. Parlanti et al. 2025b; P. G. Pérez-González et al. 2025; S. Zamora et al. 2025b), including the discovery of dual/multiple AGN (M. Perna et al. 2025; H. Übler et al. 2025). A robust characterization of the true nature of such systems is challenging without IFU spectroscopy (F. D'Eugenio et al. 2025d).

At higher redshifts, galaxies are, on average, smaller than their low-z counterparts, as demonstrated by observations (e.g. T. Shibuya, M. Ouchi & Y. Harikane 2015; M. Huertas-Company et al. 2024; J. Matharu et al. 2024; T. B. Miller et al. 2025; H. M. O. Stephenson et al. 2025; L. Yang et al. 2025; A. L. Danhaive et al. 2026b) and recent simulations (e.g. W. J. Roper et al. 2022; L. Costantin et al. 2023; X. Shen et al. 2024; W. McClymont et al. 2025). Resolving the ISM in such compact early galaxies is therefore difficult, except in cases where gravitational lensing provides sufficiently high magnification to resolve otherwise inaccessible physical scales (L. Mowla et al. 2022; A. Claeyssens et al. 2023; E. Vanzella et al. 2023; T. Y.-Y. Hsiao et al. 2024a; L. Mowla et al. 2024; S. Fujimoto et al. 2025b). Furthermore, additional caution is needed when interpreting metallicity gradients and ISM properties in high-z targets because a substantial fraction of them either consist of multiple clumps (O. Le Fèvre et al. 2020; R. Herrera-Camus et al. 2025) or are observed during a merger event (as expected given the increasing merger rates at higher redshifts; Q. Duan et al. 2025; D. Puskás et al. 2025b) during which gas and metals are redistributed across the system.

MACS0647-JD is a star-forming galaxy (SFG) at $z_{\rm spec} = 10.17$ (T. Y.-Y. Hsiao et al. 2023, 2024a), with a stellar mass of $\log(M_*/{\rm M}_\odot) = 8.1 \pm 0.3$. Its instantaneous SFR, ${\rm SFR}_{\rm H\alpha} = 5.0 \pm 0.6$ ${\rm M}_\odot$ ${\rm yr}^{-1}$ (T. Y.-Y. Hsiao et al. 2024b, probed by Hα ((narrow-line emission) places this galaxy 0.6–0.8 dex above the star-forming main sequence at its redshift (e.g. W. McClymont et al. 2025), implying that the galaxy is undergoing a starburst episode. The system is triply lensed by the foreground galaxy cluster MACSJ0647.7+7015 ($z = 0.597$; H. Ebeling et al. 2007). In this study, we analyse the image with the highest magnification, MACS0647-JD1 ($\mu = 8 \pm 1$; B. M. Y. Chan et al. 2017). This system consists of two closely separated main components (MACS0647-JD A and B) with a third component (C) located farther away from this pair (T. Y.-Y. Hsiao et al. 2023). It was furthermore determined (based on integrated aperture spectroscopy) that component A of the system has a gas-phase metallicity of $12 + \log({\rm O/H}) = 7.79 \pm 0.09$ (T. Y.-Y. Hsiao et al. 2024b) and an ionization parameter of $\log U = -1.9 \pm 0.2$, indicating a metal-poor but strongly ionized ISM, in line with other high-redshift observations (A. J. Bunker et al. 2023; M. Castellano et al. 2024; M. Curti et al. 2025). However, no conclusion has been reached about the kinematic properties and the interactions between the two main components of this system, leaving open the question of whether they are distinct components of a merger or simply gas

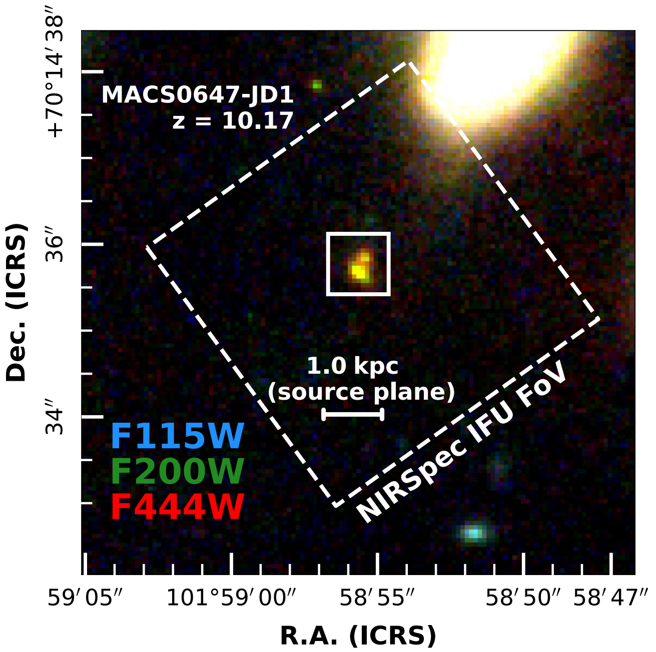

Figure 1. Composite RGB image of MACS0647-JD1 obtained by superposing *F*115*W*, *F*200*W*, and *F*444*W* NIRCam photometry images. We also overlay the field of view of our IFU observations (dashed square), as well as the central 0.7 arcsec × 0.7 arcsec aperture (solid square), used for determining the integrated spectrum emission-line fluxes and ISM properties. As discussed in Section 3.2, we only fit the emission lines in the spectra of the spaxels contained within this aperture.

clumps in a rotating disc. In this work, we present NIRSpec/IFU medium-resolution spectroscopy of this target and argue that the former scenario is more likely.

This paper is organized as follows. In Section 2, we discuss the data reduction pipeline, outlining the pre-processing applied to the raw data before using it in our analysis. Section 3 describes our point-spread-function (PSF) matching algorithm for spaxel spectra and the methods that we used to fit emission lines in the datacube, both spaxel by spaxel, as well as in spectra extracted from custom apertures. Section 4 also presents various components of our analysis and highlights the key results. Section 5 discusses the most probable nature of the MACS0647-JD system based on its resolved SFHs, gas kinematics, and ISM properties. Our conclusions are outlined in Section 6. We assume a flat Lambda-cold dark matter cosmology with $H_0 = 67.4$ km s^{-1} Mpc^{-1} and $\Omega_{\rm m} = 0.315$ (Planck Collaboration VI 2020), giving a physical scale of 4.2 kpc arcsec^{-1} at a redshift of $z = 10.17$ (before applying the lensing correction), corresponding to 1.5 kpc arcsec^{-1} in the source plane (for our assumed magnification of $\mu \sim 8$). Stellar masses refer to the total stellar masses formed, assuming a G. Chabrier (2003) initial mass function (IMF), integrated between 0.1 and 120 $M_{\odot}$. All magnitudes are in the AB system: AB mag $= 31.4 - 2.5 \times \log F_{\rm nJy}$ (J. B. Oke & J. E. Gunn 1983), and all EWs (equivalent widths) are in the rest frame, with negative EWs corresponding to line emission. All the logarithms in this paper are base-10 logarithms: $\log \equiv \log_{10}$.

2 DATA

2.1 NIRSpec/IFU observations

MACS0647-JD (ICRS coordinates of the MACS0647-JD1 image analysed in this paper: RA = $06^{\rm h}47^{\rm m}55.746^{\rm s}$; Dec. = $+70^{\circ}14'35.93''$) was first observed with the *Hubble Space Telescope* using the Wide Field Camera 3 (R. A. Kimble et al. 2008) and the Advanced Camera for Surveys (H. C. Ford et al. 2003); at the time, it was one of the most distant photometric candidates (D. Coe et al. 2013). Spectroscopic confirmation was obtained with *JWST* 10 yr later (T. Y.-Y. Hsiao et al. 2024a). Our observations are part of the Galaxy Assembly with NIRSpec Integral Field Spectroscopy[1] (GA-NIFS; PIs: S. Arribas and R. Maiolino). GA-NIFS is a NIRSpec/IFU Guaranteed Time Observations programme, and our target is included in the *JWST* Cycle 3 Programme ID no. 4528 (PI: K. Isaak). The observations used the medium-resolution *G*395*M*/*F*290*LP* disperser/filter setup. We used a medium-cycling pattern with 8 dithers, 27 groups per integration, and one integration per exposure (with the NRSIRS2 readout mode; B. J. Rauscher et al. 2017), giving an on-source time of 4.4 h.

2.2 NIRSpec data reduction and processing

The data reduction used the *JWST* science calibration pipeline v1.17.1 with CRDS jwst_1322.pmap. To improve the quality of the datacube, we performed a number of further data processing steps, in addition to the default pipeline. The customized procedures used for flagging cosmic rays snowballs and correcting pink noise (1/*f* noise) are described in detail in M. Perna et al. (2023) and D. Kashino et al. (2023). These were applied to the Stage 1 count-rate products, before the Stage 2 and Stage 3 calibrations. For outlier removal, we used the outlier-detection algorithm described in F. D'Eugenio et al. (2024a, see also H. Übler et al. 2023) and executed after Stage 2. This is adapted from the original LACOSMIC (P. G. van Dokkum 2001) algorithm. The background subtraction follows the procedure described in R. G. Pascalau et al. (2026), but here we used Hγ and [Ne III]λ3869 to obtain the source mask. The datacube was obtained using the CUBE_BUILD algorithm with a pixel size of 0.05 arcsec and 'drizzle' weighting.

2.3 Imaging and photometry

We retrieved NIRCam photometric data from the DAWN JWST Archive v7.0 (K. E. Heintz et al. 2025). We used the v7.0 MACS0647 mosaics for the *F*115*W*, *F*150*W*, *F*200*W*, *F*277*W*, *F*356*W*, and *F*444*W* filters. These imaging data were obtained as part of the *JWST* Cycle 1 Programme ID no. 1433 (PI: D. Coe). Data reduction procedures have been described in detail by G. Brammer (2023) and F. Valentino et al. (2023). We produced 3 arcsec × 3 arcsec cutouts (similar to the IFU field of view) and applied background subtraction. We first removed bright sources using a 3σ mask produced with the SIGMACLIP algorithm from ASTROPY (Astropy Collaboration 2022). We then used BACKGROUND2D from PHOTUTILS (L. Bradley et al. 2024)

[1] https://ga-nifs.github.io/

to divide the masked cutouts into 0.35 arcsec × 0.35 arcsec regions. We used MEDIANBACKGROUND as our background estimator. The background values from neighbouring background-estimation regions are smoothed using a median filter and interpolated across the full image to produce a full 2D background image.

2.4 Astrometry re-alignment of the datacube

The field of view of the NIRSpec/IFU pointing is 3.1 arcsec × 3.1 arcsec, which is large enough to contain our target even without an accurate pointing procedure. The no-target acquisition mode provides an astrometric precision of ∼ 0.1 arcsec (M. Perna et al. 2023; H. Übler et al. 2023). Because our study focuses on spatially resolved ISM properties, we refine the NIRSpec/IFU astrometry by matching the synthetic *F444W* image obtained from the datacube to the NIRCam *F444W* imaging data. This filter was chosen because its wavelength range covers the brightest part of the rest-frame optical continuum in young stellar populations, as well as key rest-frame optical emission lines in our spectra that we aim to map and study in detail. We find an offset of 0.19 arcsec between the NIRCam astrometry and our IFU data, comparable to those found in other studies (e.g. S. Arribas et al. 2024; I. Lamperti et al. 2024; H. Übler et al. 2024; S. Fujimoto et al. 2025a, b; E. Parlanti et al. 2025b). In Fig. 2, we mark the brightest spaxel in the synthetic *F444W* image with the yellow '+' cross mark. We regard this spaxel as the centroid of the stellar continuum light. However, the peak line emission centroid for the brightest emission lines in the system, Hγ and [Ne III] λ3869 (marked with a pink '×' cross symbol) is offset by 0.1 arcsec from the stellar continuum centroid. We further discuss this spatial offset, together with the different morphologies of continuum and line emission in Section 5.

2.5 Wavelength range extension and Hβ recovery

The nominal wavelength range of NIRSpec *G395M* grating reaches $\lambda = 5.27$ µm. However, wavelengths $\lambda \lesssim 5.5$ µm are still recorded on the detector, and can therefore be recovered, which is particularly useful for the brightest emission lines at high redshifts. The possibility of extending the recovered wavelength coverage beyond the nominal range has been demonstrated by several recent studies (F. D'Eugenio et al. 2025a; A. Torralba et al. 2026 using high-resolution data; E. Parlanti et al. 2025a; F. Valentino et al. 2025 using medium-resolution data). In this work, we aim to measure Hβ, with a method similar to that implemented in F. D'Eugenio et al. (2025a), but focusing on the red end of the *G395M* grating.

At $z \sim 10.17$, Hβ emission lies at $\lambda_{\rm obs} \approx 5.43$ µm, outside the nominal wavelength range covered by the *G395M*/*F290LP* disperser/filter setup. The line is well detected because the *F290LP* filter does not suppress longer wavelengths and the transmission of the grating does not drop sharply beyond $\lambda_{\rm obs} >$ 5.27 µm (F. D'Eugenio et al. 2025a). On the other hand, the [O III] $\lambda\lambda$4959, 5007 doublet lines would fall at observed wavelengths of ≈ 5.54 and ≈ 5.59 µm, respectively. At these wavelengths, the detector efficiency decreases, suppressing the [O III] $\lambda\lambda$4959, 5007 emission, which is therefore not detected. We extract the spectra by extrapolating the flat-field curves and the wavelength calibration solution beyond the nominal range. There are only 89 spectral pixels (in the case of our medium-resolution grating) between the observed wavelength of Hβ and

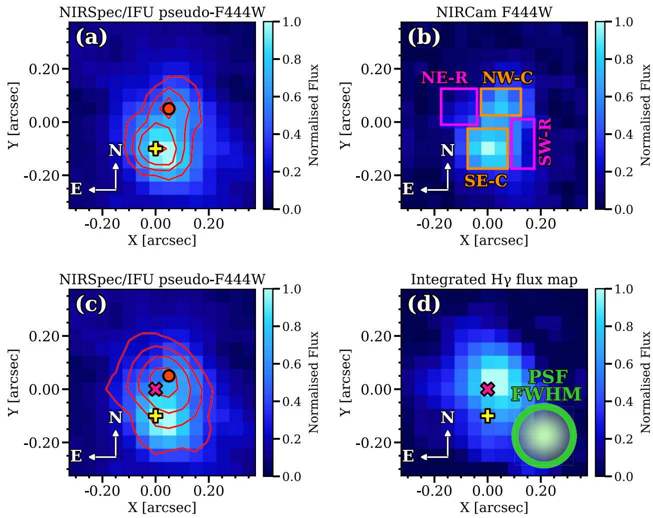

Figure 2. The top panels show the astrometric alignment between the ICRS coordinates of the NIRSpec/IFU synthetic *F444W* image (Fig. 2a) and the NIRCam *F444W* photometry (b). In (a), we overlay contours (solid, red curves) from the normalized NIRCam imaging data at 0.3, 0.5, 0.7, and 0.9 times the peak flux (defined by the stellar continuum centroid). We highlight the brightest spaxels in the two clumps in the system: south-east (yellow '+' cross) and north-west (red circle). The orange rectangles in (b) approximately mark the apertures corresponding to the SE-C and NW-C, while the magenta rectangles indicate the regions outside the main stellar components. In (c), we overlay the contours from the normalized Hγ integrated flux map (at the same fractional levels as in the top-left panel) on the synthetic *F444W* image from the datacube. We highlight the centroids of the SE-C and NW-C (yellow '+' cross and red circle), together with the centroid of Hγ emission (pink '×' cross). All the panels are shown in arcsecond offsets relative to the Hγ emission centroid. The same coordinate convention is adopted for all our subsequent maps in this paper. We also indicate the PSF FWHM (determined as described in Section 3.1) with a circle of diameter equal to the FWHM, shown with a green edge and pale green Gaussian shading to illustrate our assumption of a 2D Gaussian PSF.

the red end of the nominal spectral range of *G395M*. As a result of the well-characterized behaviour of the grating, the error on the wavelength solution is small.

To derive the flux calibration of our extended data, we rely on extrapolating the background level. We perform an initial data reduction in which we extend the existing calibration files for the flat-field correction and flux calibration. We initially use a linear extrapolation of the existing calibrations to the range 5.27–5.55 µm. The calibrations consist of an illumination flat, a detector flat, and a spectrograph flat. After this initial step, the resulting datacube displays a sharp drop at $\lambda \gtrsim 5.35$ μm. This is shown in Fig. 3(a), where the grey spectrum was extracted in an empty circular aperture from the initial datacube. Since the signal in this region is expected to increase smoothly with wavelength, we use data in the well-calibrated spectral region $\lambda < 5.27$ μm to model the background (black line) and to derive an extended flux-calibration term, $f_{\rm cal}$, defined as the ratio between the extrapolated model background and the smoothed data. This additional term rises rapidly at $\lambda \gtrsim 5.35$ μm (as shown in Fig. 3c), while at $\lambda \lesssim 5.27$ μm it oscillates between 1.00 ± 0.02 (Fig. 3b). We consider the latter oscillations to be artefacts of our background model; hence, our additional flux-calibration term is equal to unity at $\lambda \leq 5.27$ µm and is equal to the derived $f_{\rm cal}$ at $\lambda >$ 5.27 µm.

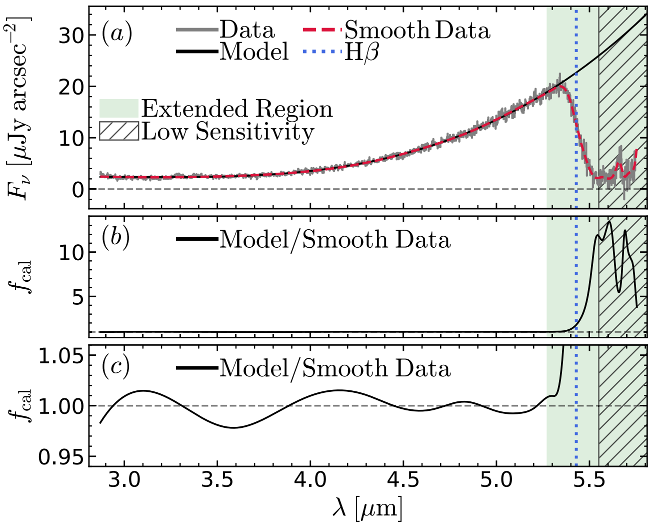

Figure 3. In (a), we display the raw and smoothed spectra from the circular aperture discussed in the main text in Section 3.2, together with the extrapolation towards longer wavelengths, outside the nominal wavelength range, but where the detector is still sensitive enough for us to extract meaningful data. (b) Illustrates the variation of the derived flux calibration factor $f_{\rm cal}$ across the wavelength range; we zoom in to $f_{\rm cal} \sim 1$ in (c).

3 ANALYSIS

3.1 PSF matching for individual spaxels spectra

In the case of individual spaxels (0.05 arcsec × 0.05 arcsec), it is crucial to take into account the size of the NIRSpec/IFU PSF. We assume the PSF to be a 2D Gaussian, allowing for the observed asymmetry in the directions along and perpendicular to the IFU slices. The first such determination of the NIRSpec/IFU PSF size was performed by F. D'Eugenio et al. (2024a) using three different methods that yielded consistent results. The authors report that the major axis of the 2D PSF is preferentially aligned with the cross-dispersion direction (corresponding to the long dimension of the slices). However, we can estimate the expected axial ratio of the PSF using the parametrization in eqs (3) and (4) from F. D'Eugenio et al. (2024a). We find that, for our wavelength range of interest 4 μm $< \lambda_{\rm obs} <$ 5.3 μm, the difference between the PSF sizes along and perpendicular to the direction of the slicers is less than 10 per cent. It is therefore reasonable to approximate the PSF shape as circular with the FWHM (full width at half-maximum) given by the geometric mean of the PSF FWHM values along and across the slicers.

In a more recent work, G. C. Jones et al. (2026a) compared the wavelength-dependent PSF FWHM predicted by the STPSF software[2] with PSF sizes estimates based on observations of two M-type stars and one white dwarf star in calibration programmes, as well as point-like quasi-stellar objects from M. A. Marshall et al. (2023, 2025b). G. C. Jones et al. (2026a) found a good agreement between these measurements and the STPSF calculations. Consequently, we use the PSF sizes determined by STPSF throughout our analysis. The emission line with the longest wavelength in our study is Hβ, and the PSF FWHM at this observed wavelength (∼ 5.43 μm) is 0.22 arcsec. Thus, we chose to PSF-match our spectra to FWHM$_{\rm PSF,max}$ = 0.22 arcsec ($\sigma_{\rm PSF,max}$ = 0.093 arcsec). First, we retrieve the PSF sizes at all wavelengths in our datacube, $\sigma_{\rm PSF}(\lambda)$. The parametrization we used was obtained by fitting the same functional form for $\sigma_{\rm PSF}(\lambda)$ as in F. D'Eugenio et al. (2024a):

$$\sigma_{\rm PSF}\,[\rm arcsec] = 0.076 + 0.013\ \times \lambda\,[\mu m] \times \exp\left(-7.6/\lambda\,[\mu m]\right) \quad (1)$$

At each wavelength, we construct a 2D circular Gaussian kernel, $\mathcal{K}(\lambda)$, with a dispersion $\sigma_K(\lambda) = \sqrt{\sigma^2_{\rm PSF,max} - \sigma^2_{\rm PSF}(\lambda)}$. We convolve the collapsed images of the datacube at each wavelength λ with $\mathcal{K}(\lambda)$, and the collapsed variance datacube slices with $\mathcal{K}^2(\lambda)$ using the CONVOLVE_FFT routine from ASTROPY.

3.2 Emission-lines-fitting procedure

We consider a square aperture of 0.7 arcsec × 0.7 arcsec centred on the Hγ emission centroid, and fit only the spaxels inside this aperture. This aperture contains most of the stellar continuum light (as shown in Fig. 1) and the fluxes of key rest-frame optical lines (as shown in Fig. A1). We do not correct for aperture losses, as we estimate them to be $\lesssim$ 10 per cent at $\lambda_{\rm obs} \sim 4-5$ μm. This expectation is based on the calculations of B. Rodríguez Del Pino et al. (2026) for a circular aperture of radius $r \sim 0.4$ arcsec, which is comparable to the half-width of our square aperture and larger than the PSF FWHM at these wavelengths (0.21 − 0.22 arcsec, as argued in Section 3.1). We show the aperture spectrum in Fig. 4(a), covering the wavelength range 3600 Å $< \lambda_{\rm rest} <$ 4700 Å. The key emission lines that we study are the [O II] λλ3726, 3729 doublet, the [Ne III] λλ3869, 3968 doublet, Hδ, Hγ, the [O III] λ4363 auroral line, and Hβ (see Section 2.5 for details on how it was extracted). Hη is not detected, as expected given the high order of this Balmer transition. Hζ and He I λ3889 are blended so we perform a crude deblending by adopting a truncated Gaussian prior on the Hδ/Hζ ratio. The prior is centred on the case-B value of Hδ/Hζ = 2.46, computed using PYNEB (V. Luridiana, C. Morisset & R. A. Shaw 2015). This is a reasonable assumption because the system does not have significant dust attenuation (as discussed in Section 4.3). We choose a standard deviation of 0.3 for this Gaussian prior because it is sufficiently broad to account for our most pessimistic estimates of the flux calibration uncertainties (∼ 10 per cent − 15 per cent). We selected Hδ because it is the closest Balmer line to Hζ that is not blended. [Ne III] λ3968 and Hϵ are blended, but we can recover their fluxes by fixing [Ne III] λ3968/ [Ne III] λ3869 = 0.301 (e.g. R. Tripodi et al. 2024; G. C. Jones et al. 2026b). All emission lines are fitted with a Gaussian profile; we tie the kinematics (the centroid and the intrinsic dispersion) of all lines. We fit the emission lines from [O II] λλ3726, 3729 to [O III] λ4363. We clip and mask $> 3\sigma$ outliers (in line-free spectral regions) in the aperture and spaxel spectra, using the SIGMA_CLIP procedure from ASTROPY (Astropy Collaboration 2022).

We explored several parametriZations for the underlying continuum, including low-order polynomials and power-law models, but found strong degeneracies among the parameters governing the continuum shape in these approaches. These issues are avoided by adopting a PPXF (M. Cappellari 2017, 2023) fit for the continuum. In this work, we used templates built using Flexible Stellar Population Synthesis (FSPS) v3.2[3] (C. Conroy et al. 2009; C.

[2] https://stpsf.readthedocs.io/en/latest/

[3] https://github.com/cconroy20/fsps

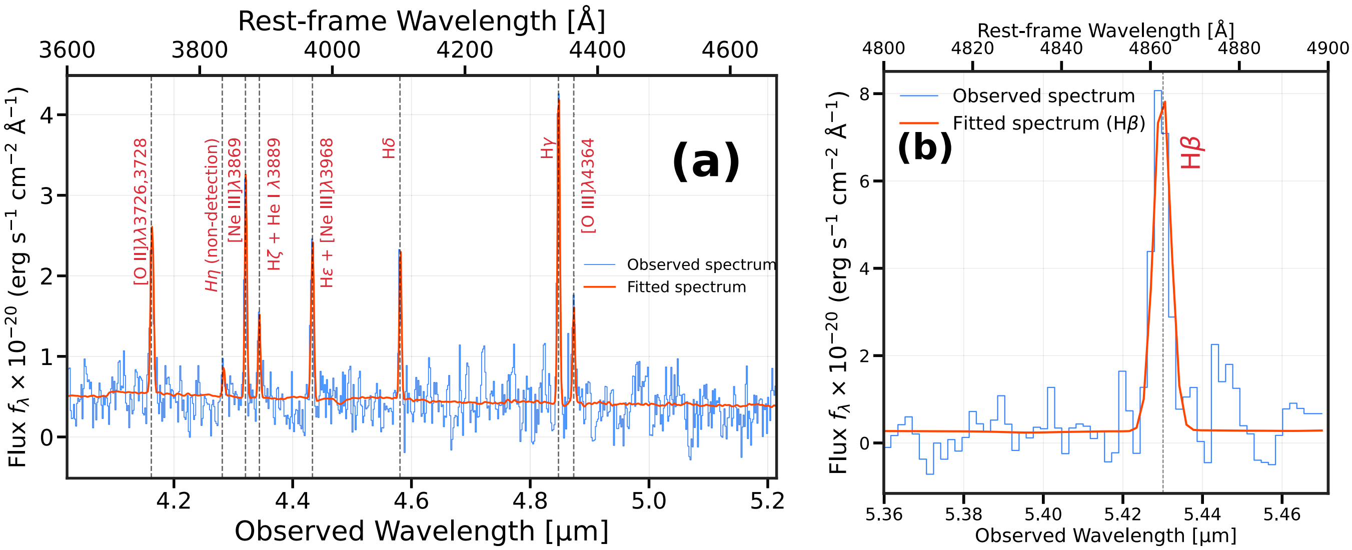

Figure 4. (a) Shows the observed integrated aperture spectrum in the rest-frame wavelength range between 3600 and 4700 Å, highlighting the key emission lines discussed in the main text, including the [O II] doublet and blended features. (b) Represents a zoom-in over the spectral wavelength range 4800 Å $< \lambda_{\rm rest} <$ 4900 Å, which, for $z = 10.17$, is redder than the nominal wavelength coverage of NIRSpec/*G395M* (2.87 − 5.27 μm). The plot highlights the best fit of the Hβ line assuming only one Gaussian component, constrained by the kinematics of multiple emission lines shown in the left panel.

Conroy & J. E. Gunn 2010), with the MILES stellar library for the optical region (P. Sánchez-Blázquez et al. 2006; J. Falcón-Barroso et al. 2011) and the MIST isochrones (J. Choi et al. 2016). We adopted a G. Chabrier (2003) IMF. During the continuum fitting, spectral regions within ±10 Å of the rest-frame wavelengths of the main emission lines indicated in Fig. 4 were masked to prevent nebular emission from biasing the stellar continuum and absorption modelling. The continuum was fitted in the unmasked regions using both stellar and gas templates; the latter were kept enabled to account for possible residual contributions from faint nebular lines not included in the main emission-line mask. It is important to note, however, that the stellar continuum in our data is intrinsically very weak, and as a result the continuum fit does not strongly constrain detailed stellar population properties. Consistent with this, the underlying stellar Balmer absorption features are modest: in the full-aperture spectrum we measured rest-frame equivalent widths of EW(Hγ) ≈ 0.36 Å and EW(Hδ) ≈ 0.57 Å in the best-fitting stellar model. These values imply that uncertainties in the modelling of the continuum and stellar absorption features have a negligible impact on the emission-line fluxes (which are calculated at a later step), which represent the core part of our analysis.

To take into account the possible systematics in the errors measured within the pipeline, we rescaled the nominal flux uncertainties (extracted from the datacube ‘ERR’ extension file) such that the median value of the noise in a given spaxel (measured across wavelength slices free of emission lines) matches the standard deviation of the residuals from the spectral fit in the line-free spectral regions. Because the noise rescaling factor is not known beforehand, we allowed it to be a free parameter in our fitting algorithm. A similar noise rescaling approach was implemented by G. C. Jones et al. (2025a) in their study of a $z \sim 4.26$ rotating disc SFG. For individual spaxels, rescaling factors vary between 1.9 and 2.5 (H. Übler et al. 2023, 2024; G. Venturi et al. 2025). Finally, in the case of aperture spectra (obtained by adding the spectra of individual spaxels within each aperture), we obtain the uncertainties by adding in quadrature the rescaled uncertainties in the spaxel spectra.

We first identify the minimum χ^2 solution of our emission-line-fitting algorithm using a least-squares procedure. To deconvolve the intrinsic line profiles from the observed features, we assume that the wavelength-dependent line spread function (LSF) of NIRSpec is given by the nominal, pre-launch resolution, $\mathrm{FWHM}_{\mathrm{LSF\ pre\text{-}launch}}$ (P. Jakobsen et al. 2022), assumed to be Gaussian and improved by a factor of 0.8, following A. J. Shajib et al. (2025, and roughly in agreement with e.g. J. E. Greene et al. 2024). The pre-launch estimates for the LSF width were too conservative because *JWST* provides a lower than expected wavefront error. The intrinsic $\mathrm{FWHM}_{\mathrm{intr}}$ is thus:

$$\mathrm{FWHM}_{\mathrm{intr}} = \sqrt{\mathrm{FWHM}^2_{\mathrm{obs}} - \left(0.8 \times \mathrm{FWHM}_{\mathrm{LSF\ pre\text{-}launch}}\right)^2}\,. \qquad (2)$$

After this step, we use the least-squares solution to initialize the chains used to compute the posterior distributions of our models using a Markov Chain Monte Carlo (MCMC) method and the software EMCEE (D. Foreman-Mackey et al. 2013). The fiducial parameters are the median values of the marginalized posterior distributions, and the uncertainties are derived from the 16th and 84th percentiles. We assumed flat priors on all parameters and set the following prior bounds: $0 < \log\left(F_{\rm int}/10^{-20}\ \mathrm{erg\,s^{-1}cm^{-2}}\right) < 3$ for integrated fluxes, $10.15 < z < 10.20$ and $100\ \mathrm{km\,s^{-1}} < \mathrm{FWHM} < 500\ \mathrm{km\,s^{-1}}$. For the ratio [O II] λ3729/[O II] λ3726, we assume a range of [0.34, 1.5] (R. L. Sanders et al. 2016). We fitted the two [O II] λλ3726, 3729 doublet components individually and tied their kinematics to those of other features (including the other, non-blended features). We note that, although we fitted the [O II] λλ3726, 3729 doublet components individually and tied their kinematics to those of other, non-blended features, our medium-resolution data cannot fully break the degeneracy between the red-to-blue line ratio [O II] λ3729/ [O II] λ3726 and the flux of the blue component. However, the total [O II] λλ3726, 3729 flux is well constrained and we will focus on this parameter from now on.

Additionally, we tested an alternative fitting model for the integrated aperture spectrum in which we assumed that all emission lines are fitted with two Gaussians from two sets of kinematically tied components. The broader Gaussians are allowed to vary over a range of $100\ \mathrm{km\ s^{-1}} < \mathrm{FWHM} < 1000\ \mathrm{km\ s^{-1}}$. However, a simple Bayesian Information Criterion (BIC; G. Schwarz 1978) test yields that $\Delta\mathrm{BIC} \equiv \mathrm{BIC}_{2\ \mathrm{comp}} - \mathrm{BIC}_{1\ \mathrm{comp}} \approx 11$. Hence, the two-Gaussians model is statistically disfavoured relative to the single-Gaussian model (even in the high-S/N aperture spectrum). We repeated this analysis for the spaxel spectra in the wavelength range $3600\ \mathrm{Å} < \lambda_{\mathrm{rest}} < 4700\ \mathrm{Å}$, but found that no spaxel simultaneously satisfied both $\Delta\mathrm{BIC} < -10$ (which would indicate that a two-component fit is statistically favoured), and $\mathrm{S/N} > 3$ for the secondary, high-FWHM component. Therefore, it is reasonable to adopt single-Gaussian fits for all spaxels. Hβ is fitted separately from the other rest-frame optical emission lines, given the higher uncertainties of the continuum at $\lambda_{\mathrm{obs}} > 5.27\ \mu\mathrm{m}$, outside the nominal range covered by *G395M*/*F290LP*. The kinematics of Hβ were tied to the lower wavelength lines by imposing the posteriors of redshift and FWHM (derived from our $3600\ \mathrm{Å} < \lambda_{\mathrm{rest}} < 4700\ \mathrm{Å}$ emission-line fit) as the priors on the Hβ redshift and FWHM. This approach allows some flexibility in deriving the Hβ kinematics and better accounts for possible wavelength calibration uncertainties than simply fixing $z_{\mathrm{H}\beta}$ and $\mathrm{FWHM}_{\mathrm{H}\beta}$ to the median values of the posterior distributions from the $3600\ \mathrm{Å} < \lambda_{\mathrm{rest}} < 4700\ \mathrm{Å}$ fit. Only the Hβ flux was fitted as a free parameter with a flat prior distribution.

Following these methods, we obtain the integrated aperture spectra over the $3600\ \mathrm{Å} < \lambda_{\mathrm{rest}} < 4700\ \mathrm{Å}$ wavelength range (Fig. 4a) and in the spectral region around Hβ (Fig. 4b). The latter allows us to estimate the uncertainties in our flux calibration outside the nominal wavelength range of the G395M/F290LP setup. We estimate an integrated Hβ flux of $(3.69 \pm 0.23) \times 10^{-18}\mathrm{erg\ s^{-1}\ cm^{-2}}$ from the full-aperture spectrum (shown in Fig. 4b). T. Y.-Y. Hsiao et al. (2024b) presented MIRI/MRS IFU (Mid InfraRed Instrument, Medium Resolution Spectroscopy Integral Field Unit) observations of the MACS0647-JD1 lensed image of our target but did not detect Hβ directly. The authors estimated an Hβ flux of $(3.29 \pm 0.37) \times 10^{-18}\ \mathrm{erg\,s^{-1}\,cm^{-2}}$ by extrapolating from the detected Hα flux of $(9 \pm 1) \times 10^{-18}\ \mathrm{erg\,s^{-1}\,cm^{-2}}$ and assuming a case-B ratio of Hα/H$\beta \sim 2.74$ at $T_{\mathrm{e}} = 20\,000\ \mathrm{K}$. While it is possible that a small amount of dust may be present, its effect on the inferred Hβ flux would be much smaller than the error bars on the flux measurement itself (as we argue in more detail in Section 4.3). We therefore conclude that, within the associated uncertainties, the Hβ flux inferred by T. Y.-Y. Hsiao et al. (2024b) is consistent with the full-aperture Hβ flux in our datacube. This suggests that the flux calibration uncertainties in the extended spectral region of the datacube are less than ~ 15 per cent.

Using the same methods described above, we obtained the line ratios maps for $\mathrm{O_3Hg} \equiv \log\,([\mathrm{O\,III}]\,\lambda4363/\mathrm{H}\gamma)$ and $\mathrm{Ne_3O_2} \equiv \log\,([\mathrm{Ne\,III}]\,\lambda3869/\,[\mathrm{O\,II}]\,\lambda\lambda3726,\,3729)$. These are displayed in Figs 5(a) and (b), respectively, together with the gas FWHM map in Fig. 5(d).

3.3 Combined SED fitting of photometry and spectroscopy

To study the link between the spatially resolved ISM properties and SFHs, we measure the stellar-population properties of the MACS0647-JD system using PROSPECTOR, a Bayesian SED (Spectral Energy Distribution) modelling tool (B. D. Johnson et al. 2021), built around the FSPS (C. Conroy et al. 2009; C. Conroy & J. E. Gunn 2010) tool. We fit the NIRCam photometry and NIRSpec/*G395M* spectroscopy of MACS0647-JD1 simultaneously for all spaxels in the cutout described in Section 3.2. We use the MILES stellar spectral library (P. Sánchez-Blázquez et al. 2006; J. Falcón-Barroso et al. 2011) and the MIST isochrones (J. Choi et al. 2016). Our stellar mass prior is informed by the observed stellar mass function (B. Wang et al. 2023a; Q. Duan et al. 2026a), and the composite stellar populations are constructed as in the PROSPECTOR-β model (B. Wang et al. 2023a). The stellar metallicity follows a truncated Gaussian prior, $\log\,(Z_*/Z_\odot) \sim \mathcal{N}\,(-1.0;\ 0.5)$, truncated to $[-2.0;\ 0.0]$. We adopt a flexible non-parametric SFH continuity prior (J. Leja et al. 2019) with eight age bins. Nebular emission is modelled using CLOUDY (v13.03; G. J. Ferland et al. 2013, 2017) as implemented in FSPS (N. Byler et al. 2017). Dust attenuation is modelled using the two-component model of S. Charlot & S. M. Fall (2000), with a diffuse dust component optical depth $\tau_2 \sim \mathcal{N}\,(0.3;\ 1)$, truncated to $[0;\ 4]$, and a birth-cloud-to-diffuse dust ratio $\tau_1/\tau_2 \sim \mathcal{N}\,(1;\ 0.3)$, truncated to $[0;\ 2]$. The attenuation curve slope n_{dust} is drawn from a uniform prior over $[-1.2;\ 0.4]$ (S. Noll et al. 2009). We do not include dust emission in our model, as it is negligible at the rest-frame wavelengths $\lesssim 5000\ \mathrm{Å}$ probed here. We also account for absorption by the intergalactic medium following the prescription of A. K. Inoue et al. (2014). To account for flux calibration and slit-loss effects, we model the spectral response using an eighth-order polynomial distortion that allows the observed spectrum to match the continuum shape predicted by the SED model. We additionally include a single jitter parameter that rescales the

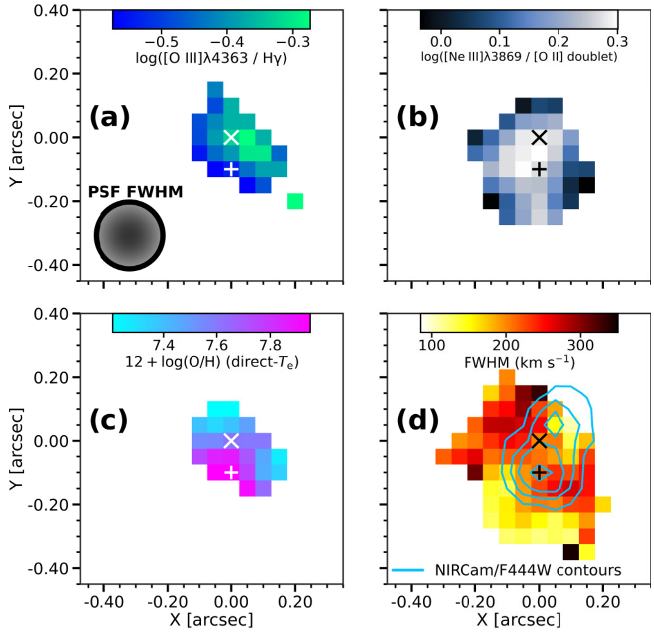

Figure 5. Top panels: maps of the diagnostic ratios $\mathrm{O_3Hg}$ and $\mathrm{Ne_3O_2}$ (allowing only spaxels with $\mathrm{S/N} > 3$ for each emission line involved). The bottom panels show the spaxel-by-spaxel maps of gas-phase metallicity (c; showing only the spaxels with $\mathrm{S/N} > 3$ for [O III] λ4363, Hγ, and inferred [O III] λ5007) and the intrinsic, deconvolved gas FWHM (d; we only show spaxels with a $\mathrm{S/N} > 5$ detection of Hγ). The FWHM map shows two high-dispersion regions which coincide with the locations of the metal-poor gas. The '×' and '+' crosses mark the Hγ emission line and the *F444W* stellar continuum centroids, respectively (as in Fig. 2). We also show the PSF size on the top-left panel for comparison.

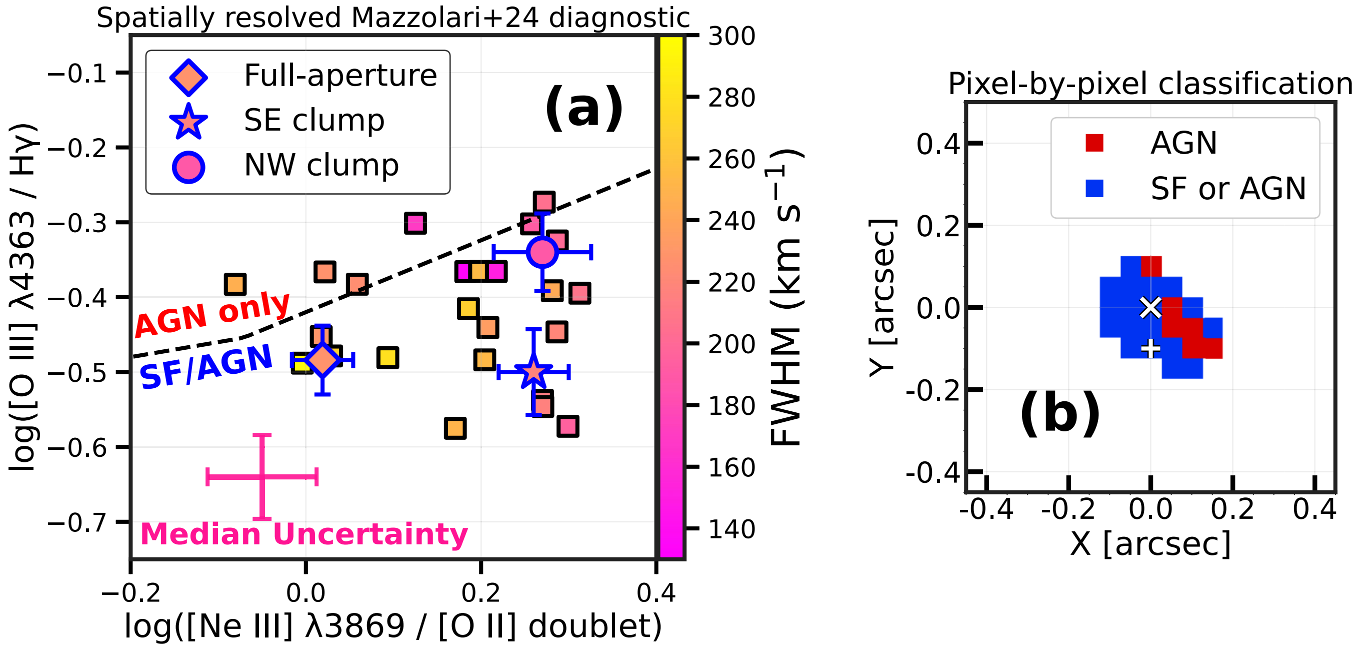

Figure 6. (a) Illustrates the position of individual spaxels on the O_3Hg versus Ne_3O_2 diagnostic diagram from G. Mazzolari et al. (2024). The dashed demarcation line separates regimes that are fully dominated by AGN photoionization (AGN only) from regions in which both AGN and/or star formation may have similar contributions. Squares are individual spaxels, colour coded by the FWHM from the single Gaussian component fit. We only show the pixels in which S/N > 5 for Hγ and [Ne III] λ3869 and S/N > 3 for [O III] λ4363 and for [O II]. The pink error bars from the bottom-left corner of the left panel are the median uncertainties from spaxels measurements. The ratios from the full-aperture, NW-C and SE-C spectra lie below the demarcation line. On the spatially resolved map (b), we identify the spaxels with either AGN or SF/AGN classification.

spectral uncertainties, capturing residual calibration systematics, and ensuring a statistically consistent fit. Overall, the model configuration and prior choices are motivated by a broad range of previous studies of high-redshift galaxies (e.g. J. Leja et al. 2019; S. Tacchella et al. 2022a, b, 2023; Q. Duan et al. 2024; T. Harvey et al. 2025).

We present our results in Section 5.4, where we discuss the implications of the spatial distributions of stellar mass and star formation burstiness, defined as SFR_{10}/SFR_{100}, the ratio of the star formation rates averaged over lookback time-scales of 10 and 100 Myr. We report the SFHs and the corner plots showing the posterior distributions and the correlations between various SED parameters for the two main stellar components (Figs D1 and D2 in Appendix D).

4 RESULTS

4.1 Identification of AGN-dominated spaxels

To constrain the dominant ISM excitation mechanism, we use the star-forming/AGN diagnostic diagram from G. Mazzolari et al. (2024), which can classify spectra as AGN-only, or consistent with both AGN and star formation. These diagnostics are commonly used in studies of high-redshift AGN (e.g. G. Mazzolari et al. 2025; S. Geris et al. 2026; L. R. Ivey et al. 2026b; I. Juodžbalis et al. 2026). We focus on the emission-line ratios O_3Hg and Ne_3O_2. According to eq. (5) of G. Mazzolari et al. (2024), the 'AGN-only' scenario is disfavoured for the integrated spectrum of MACS0647-JD1 and the SE clump (SE-C), but it is consistent within the 1σ uncertainties for the NW clump (NW-C). A number of spaxels in the south-west region (SW-R) are identified as AGN dominated, lying above the demarcation line from Fig. 6(b), and others lie below the demarcation line, but still close to it (Fig. 6a). Given the large error bars and the predominant location of 'AGN-only' spaxels away from the centre, we disfavour an AGN interpretation.

Supporting this interpretation, no spaxel is identified as purely dominated by AGN if we instead use the $O_3Hg - O_{32}$ or $O_3Hg - O_{33}$ ($\equiv$ log([O III] λ5007/ [O III] λ4363) diagnostics (as shown in Fig. B1 in Appendix B). However, in this case, the uncertainties are larger than for the previous diagram because: (i) both the O_{32} and O_{33} ratios require a reddening correction, and (ii) our spatially resolved [O III] λ5007 fluxes are obtained using the extrapolation method described in Section 4.2. In summary, we disfavour, although do not completely rule out, an AGN interpretation.

4.2 Direct-method gas-phase metallicities

To calculate the electron temperatures from the spectra of individual spaxels (which are required to infer the direct-T_e metallicities), we need to estimate the [O III] λ5007 fluxes. We use eq. (1) from J. Witstok et al. (2021), which connects the observed [O III] λ5007 / [O II] $\lambda\lambda$3726, 3729 and [Ne III] λ3869 / [O II] $\lambda\lambda$3726, 3729 ratios for SFGs:

$$\log\left(\frac{[\mathrm{O\,III}]\,\lambda5007}{[\mathrm{O\,II}]\,\lambda\lambda3726,3729}\right) = 0.905\log\left(\frac{[\mathrm{Ne\,III}]\,\lambda3869}{[\mathrm{O\,II}]\,\lambda\lambda3726,3729}\right) + 1.078. \qquad (3)$$

In this paragraph, we discuss possible caveats. This empirical conversion relation has a mean scatter of 0.22 dex, calculated based on the full sample of SDSS (Sloan Digital Sky Survey) SFGs (K. N. Abazajian et al. 2009). However, the subset of galaxies with a higher ionization parameters (log ([Ne III] λ3869/ [O II] $\lambda\lambda$3726, 3729) > $-$1; a regime that is more common in the case of high-z, low-metallicity galaxies) have a scatter of 0.12 dex around the J. Witstok et al. (2021) equation. As a conservative approach, we propagate this source of uncertainty by adding 0.22 dex in quadrature to the numerical uncertainties associated with the [O III] λ5007 fluxes (for integrated-aperture or individual spaxels spectra). Another possible caveat is that equation (3) is mainly valid for SF-dominated (rather than AGN-dominated) spaxels. However, we notice (based on Figs 6b and 5b) that the AGN-dominated spaxels all have $Ne_3O_2 > 0.08$, a regime in which the [O III] λ5007 / [O II] λλ3726, 3729 – [Ne III] λ3869 / [O II] λλ3726, 3729 empirical conversion relations for SFGs and Seyfert-1 galaxies are offset by $\lesssim 0.03$ dex (fig. 4 of J. Witstok et al. 2021). This source of systematic uncertainty is therefore negligible compared to, for example, the mean scatter of the empirical relation itself. We can therefore reasonably adopt the [O III] λ5007 fluxes predicted by equation (3). This method of estimating the flux of [O III] λ5007 has also been used by several studies of the physical properties of the ISM (including the metallicity and ionization parameter) in $z > 10$ galaxies (A. J. Bunker et al. 2023; J. Scholtz et al. 2026). Although the empirical equation (3) was derived using $z \sim 0$ galaxies from SDSS, such a correlation between [O III] λ5007 / [O II] λ3726, 3729 and [Ne III] λ3869 / [O II] λ3726, 3729 has recently been shown to exist at least up to $z \sim 9.5$, as illustrated in fig. 6 of S. Zamora et al. (2025a), based on a compilation of $z > 5$ *JWST* observations (K. Z. Arellano-Córdova et al. 2022; A. J. Cameron et al. 2023; M. Curti et al. 2023, 2025; R. L. Sanders et al. 2023a; K. E. Heintz et al. 2024; D. Schaerer et al. 2024; M. W. Topping et al. 2024). For the integrated-aperture spectrum of MACS0647-JD1, the inferred [O III] λ5007 line flux is $(2.24 \pm 0.52) \times 10^{-17}$ erg s^{-1} cm^{-2}, consistent with the value obtained from MIRI medium-resolution spectroscopy of this target (T. Y.-Y. Hsiao et al. 2024b). This result demonstrates the potential of the method proposed by J. Witstok et al. (2021) to extrapolate [O III] λ5007 based on [Ne III] λ3869 at $z > 10$, where [O III] λ5007 falls outside the wavelength range of NIRSpec.

The electron temperature is calculated using [O III] λ4363/ [O III] λ5007. We first assume that dust attenuation is negligible ($A_{\rm V,cont} \lesssim 0.1$ mag; T. Y.-Y. Hsiao et al. 2024a). For the full aperture spectrum, PYNEB (V. Luridiana et al. 2015) predicts a mean temperature of the [O III]-emitting gas $T_{\rm e}$ [O III] $= (1.9 \pm 0.4) \times 10^4$ K for an auroral-to-strong-line ratio of 0.031 ± 0.009, assuming an electron density of 2000 cm^{-3} (as determined by Abdurro'uf et al. 2024, using high-resolution spectroscopic data for our target). We also tested a wide range of electron densities 100 cm^{-3} $< n_e <$ 10 000 cm^{-3} which extends beyond the typical range of [O II] λλ3726, 3729 based electron densities in high-redshift galaxies (Y. Isobe et al. 2023b; C. Marconcini et al. 2024; J. Scholtz et al. 2025a) and found that the dependence of our $T_{\rm e}$ [O III] estimate on the assumed $n_{\rm e}$ is negligible. A similar procedure is applied to compute the electron temperatures from the spectra of individual spaxels, and our results are displayed in Fig. 7(b).

Once we calculate our $T_{\rm e}$ [O III] values, we can determine the electron temperature of the [O II] emitting gas using eq. (14) from Y. I. Izotov et al. (2006). We then compute the gas-phase metallicities (as given by the oxygen abundances). O. L. Dors et al. (2020) showed that the contribution of O^{3+} is negligible even in highly AGN-dominated regimes. Thus, we can assume all oxygen atoms are either singly or doubly ionized in these conditions. We use [O II] λλ3726, 3729/Hβ and [O III] λ5007/Hβ to compute the abundances of the O^+ and O^{++} ions using PYNEB. For the aperture spectrum, we obtain $12 + \log({\rm O/H}) = 7.59 \pm 0.17$, in agreement with the result of T. Y.-Y. Hsiao et al. (2024b) and similar to the direct-$T_{\rm e}$ metallicities reported for a number of other SFGs at $z \sim 4 - 9$ (e.g. M. Curti et al. 2023; K. E. Heintz et al. 2023; K. Nakajima et al. 2023; T. Morishita et al. 2024). To further test the consistency of our method, (given the indirect approach used to extract Hβ fluxes), we repeat our calculation but using the ratios [O II] λλ3726, 3729/Hγ and [O III] λ5007/Hγ (instead of their counterparts involving Hβ). We obtain $12 + \log({\rm O/H}) = 7.52 \pm 0.18$ in agreement with our previous value, and acting as a cross-validation of both the method and the flux calibration. For individual spaxels, we additionally perform the dust attenuation corrections described in Section 4.3. The resulting metallicity map is shown in Fig. 5(c).

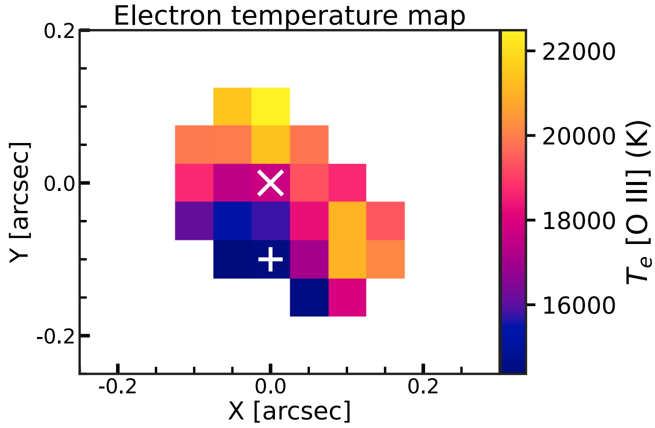

Figure 7. This figure shows the map of the electron temperature of the [O III] emitting gas in the central region of the system. We only show spaxels with S/N > 3 for the auroral [O III] λ4363 line. The white '+' and '×' crosses mark the centroids of stellar continuum and Hγ line emission, respectively.

To assess the impact of dust reddening on our calculated parameters, we adopted a stellar continuum dust attenuation following the Calzetti law (D. Calzetti et al. 2000) with $A_{\rm V,cont} =$ 1 mag for the full-aperture spectrum (although this value is unreasonably high from a physical point of view; A. Ferrara, A. Pallottini & L. Sommovigo 2025). This would imply a gas-phase metallicity of $12 + \log({\rm O/H}) = 7.71$, which is within the quoted uncertainties of our $A_{\rm V,cont} = 0$ estimate. For an assumed $A_{\rm V,cont} = 2$ mag, we obtain $12 + \log({\rm O/H}) = 7.90$. Thus, as a first-order approximation, the change in calculated metallicity and the change in assumed dust attenuation are related by $\Delta \log({\rm O/H}) / \Delta A_{\rm V,cont} \approx 0.18$ dex mag^{-1}.

4.3 Dust attenuation corrections

Various recent studies use the Balmer decrement ratios to compute the nebular dust attenuation for individual spaxels (G. Venturi et al. 2024; L. R. Ivey et al. 2026b). In our case, thanks to our custom Hβ extraction procedure (Section 2.5), the lowest order Balmer lines are Hβ and Hγ. We use PYNEB to compute the theoretical case-B Balmer ratio $({\rm H}\beta/{\rm H}\gamma)_0 = 2.105$ (assuming $T_{\rm e} =$ 19 000 K as derived in Section 4.2). The stellar continuum dust attenuation is:

$$A_{\rm V,cont} = -2.5 \times 0.44 \times \log\left(\phi_{\rm obs}/\phi_0\right) \times R_V / \left(k_{\lambda,{\rm H}\beta} - k_{\lambda,{\rm H}\gamma}\right) \,, \quad (4)$$

where the factor of 0.44 comes from the relation between stellar and nebular dust attenuation (D. Calzetti et al. 2000), and we define $\phi \equiv {\rm H}\beta/{\rm H}\gamma$. We assume $R_V = 4.05$ (D. Calzetti et al. 2000). For the dust attenuation law, we assume a slightly modified version of the Calzetti law that is suitable for low-mass, low-metallicity galaxies (I. Shivaei et al. 2020). We find that, for all spaxels considered in computing the direct-method metallicity map, except for three outliers, $A_{\rm V,cont} \lesssim 0.3$ mag (and consistent with 0 within the uncertainties) whereas the highest outlier has $A_{\rm V,cont} \approx 0.6$ mag. According to our previously calculated $\Delta\log{\rm (O/H)}/\Delta A_{\rm V,cont} \approx 0.18$ dex mag^{-1} (Section 4.2), this implies that the effect of dust attenuation correction on the derived spaxels metallicities is less than 0.11 dex. We will therefore, as a first-order approximation, correct the line ratios from spaxels spectra assuming the Calzetti dust attenuation curve with the $A_{\rm V,cont}$ derived using this method.

We now separately discuss individual spaxels with ${\rm H}\beta/{\rm H}\gamma < ({\rm H}\beta/{\rm H}\gamma)_0$ (which cannot be explained by dust attenuation assuming case-B recombination). In all but four cases of spaxels with below case-B ${\rm H}\beta/{\rm H}\gamma$ decrement ratios and S/N > 3 for Hβ, Hγ, and Hδ, we notice that the ${\rm H}\gamma/{\rm H}\delta$ remains above the corresponding case-B Balmer ratio. In principle, stronger stellar absorption in Hβ could be responsible for this behaviour (B. Groves, J. Brinchmann & C. J. Walcher 2012; S. Tacchella et al. 2023); while our PPXF continuum modelling allows for stellar absorption (as described in Section 3.2), the weakness of the continuum of our $z \sim 10.17$ target implies that any stellar absorption has a negligible impact on the measured emission-line fluxes. Moreover, potential calibration uncertainties in the extrapolated wavelength range ($\lambda_{\rm obs} > 5.27\,\mu$m) could also contribute to artificially low Hβ fluxes. Because of the wavelength proximity of Hγ and Hδ, this Balmer decrement ratio is not suitable for accurately calculating the dust attenuation, especially in low-S/N targets. As a result, we assume that $A_{\rm V,cont} = 0$ mag for these spaxels.

There are only four spaxels for which both ${\rm H}\beta/{\rm H}\gamma$ and ${\rm H}\gamma/{\rm H}\delta$ are more than 1σ below their expected case-B values and all are located west of the SE-C, in the region where we expect a non-negligible contribution from AGN (as discussed in Section 4.1). Indeed, below case-B Balmer ratios, including ${\rm H}\beta/{\rm H}\gamma$ and ${\rm H}\alpha/{\rm H}\beta$, have been reported for stacked Type-2 AGN (J. Scholtz et al. 2025b). Case-B assumptions may not be fulfilled under optically thin or non-equilibrium conditions (C. Scarlata et al. 2024). While such conditions typically require high electron temperatures and/or low electron densities, which are not indicated by our measurements, we cannot exclude localized departures from case-B assumptions in these regions. We adopt a similar approach of assuming $A_{\rm V,cont} = 0$ mag for these spaxels. We expect this assumption to have a negligible impact on the derived gas-phase metallicities, given the findings of T. Y.-Y. Hsiao et al. (2024a), who report $A_{\rm V,cont} \lesssim 0.3$ mag for the integrated aperture spectrum (covering the SE-C within the slit).

As an additional sanity check, we estimate $A_{\rm V,cont}$ based on our combined spaxel-by-spaxel PROSPECTOR SED fits (described in Section 3.3). Taking into account that both diffuse dust (optical depth τ_2) and dust from the birth clouds (optical depth τ_1) contribute to the total dust attenuation, we approximate $A_{\rm V,cont} \approx 2.5 \times 0.44 \times \log_{10}(e) \times (\tau_1 + \tau_2)$. In reality, this formula gives an upper limit on $A_{\rm V,cont}$, with the actual value depending on the exact fraction of light coming from young stars (< 10 Myr) relative to the total. Constraining this parameter is beyond the scope of this paper. From this calculation, we find that, in the case of spaxels with ${\rm S/N}_{[{\rm O\,III}]\lambda4363} > 3$, the highest $A_{\rm V,cont}$ is ~ 0.5 mag, although most spaxels have $A_{\rm V,cont} \sim 0.0 - 0.4$ mag. The values obtained for the two clumps and for the full cutout aperture are reported in Table 1. Overall, the results obtained with these methods are in agreement, illustrating the difficulty of providing accurate dust corrections on spatially resolved scales (as also mentioned by T. A. Hutchison et al. 2025). However, we demonstrate that, regardless of the dust correction method implemented, the effect on the inferred metallicities is expected to be smaller than the measurement uncertainties.

Table 1. Physical parameters of the MACS0647-JD1 system and of its main stellar components.

Parameter	Full aperture	SE clump	NW clump
Gas FWHM (km s^{-1})	228 ± 19	215 ± 34	189 ± 41
$12 + \log{\rm (O/H)}$ (dir)	7.59 ± 0.17	7.89 ± 0.16	7.47 ± 0.20
$12 + \log{\rm (O/H)}$ (str)	7.66 ± 0.14	7.71 ± 0.13	7.49 ± 0.15
$T_{\rm e}$ [O III] /10^4 K	1.90 ± 0.37	1.52 ± 0.29	$2.38^{+0.32}_{-0.40}$
$\log U$	-2.05 ± 0.07	-1.84 ± 0.06	-1.84 ± 0.09
${\rm SFR}_{{\rm H}\gamma}$ (M$_\odot$ yr^{-1})	5.5 ± 1.0	1.0 ± 0.2	0.50 ± 0.15
${\rm SFR}_{100}$ (M$_\odot$ yr^{-1})	2.9 ± 0.4	0.56 ± 0.10	0.24 ± 0.05
$\log(M_*/{\rm M}_\odot)$	8.38 ± 0.21	7.78 ± 0.07	7.41 ± 0.08
$A_{\rm V,cont}$ (PROSPECTOR)	0.26 ± 0.15	0.13 ± 0.05	0.18 ± 0.07

Notes. The top rows in this table present our results for some properties derived directly from large integrated aperture spectra and from the spectra corresponding to the SE and NW clumps. The bottom rows, on the other hand, give the values of various parameters resulting from spectrophotometric SED modelling (see Sections 3.3 and 5.4).

4.4 Gas-phase metallicities (strong-line method)

The strong nebular emission lines provide an alternative method for estimating gas-phase metallicities in high-redshift SFGs (e.g. K. Nakajima et al. 2022; M. Curti et al. 2024; E. Cataldi et al. 2025; D. Scholte et al. 2025; R. L. Sanders et al. 2026). These calibrations are valid only for SFGs and link strong emission-line ratios to metallicities based on the more reliable and more general 'direct' method. However, it is important to note that these studies use integrated aperture spectra, so they do not account for spatial variations in the ISM conditions and/or systematic physical effects (e.g. localized shocks, and AGN) that can affect the metallicity measurements on resolved scales. In this work, we choose to use the robust SFG R_3 versus Ne_3O_2 photoionization grid from J. Gutkin et al. (2016), as shown in Fig. 8. We use $R_3 \equiv \log([{\rm O\,III}]\,\lambda5007/{\rm H}\beta)$ as a primary tracer of metallicity, with [O III] λ5007 fluxes calculated based on the J. Witstok et al. (2021, eq. 3). To break the degeneracy with the ionization parameter, we additionally use Ne_3O_2 (R. Maiolino & F. Mannucci 2019). This photoionization grid method has the further advantage that both line ratios are insensitive to dust attenuation, since all the emission lines involved in our calculations have similar wavelengths.

T. Y.-Y. Hsiao et al. (2025) measure a carbon abundance of $\log{\rm (C/O)} = -0.44 \pm 0.07$ for MACS0647-JD1. Given the value of ${\rm (C/O)}_\odot = 0.44$ assumed by J. Gutkin et al. (2016), we select the grid with a carbon abundance of ${\rm (C/O)} = 0.72\,{\rm (C/O)}_\odot$ which is the closest available value to $0.82^{+0.13}_{-0.09}\,{\rm (C/O)}_\odot$ measured by T. Y.-Y. Hsiao et al. (2025). We choose an upper stellar mass cut-off for the IMF of 100 M$_\odot$ for our grid and a fiducial hydrogen gas

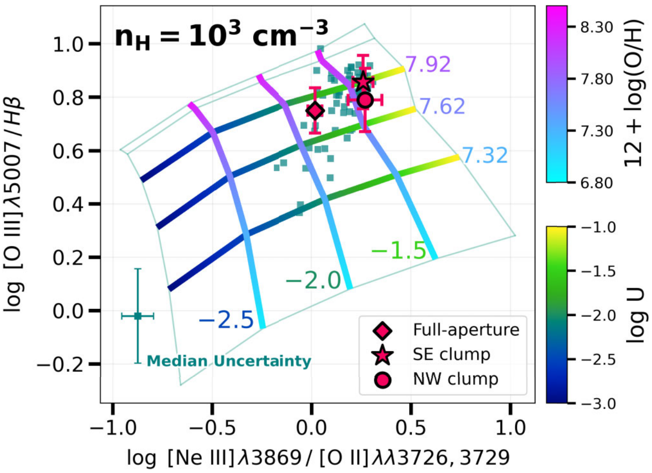

Figure 8. This figure shows the R_3-Ne_3O_2 photoionization grid (with varying metallicity and ionization parameter) of SFGs from J. Gutkin, S. Charlot & G. Bruzual (2016) based on CLOUDY models (G. J. Ferland et al. 2013, 2017). The choice of the grid is motivated in the main text of Section 4.4. Individual spaxels (with S/N > 5 on [Ne III] λ3869, [O II] λ3726, 3729, and Hβ lines) are plotted as dark-cyan small squares and their median uncertainties are shown in the bottom-left part. The circle, diamond, and star symbols denote the results from the full aperture and the two main SE and NW components. These two line ratios also offer the advantage that they do not require dust reddening correction.

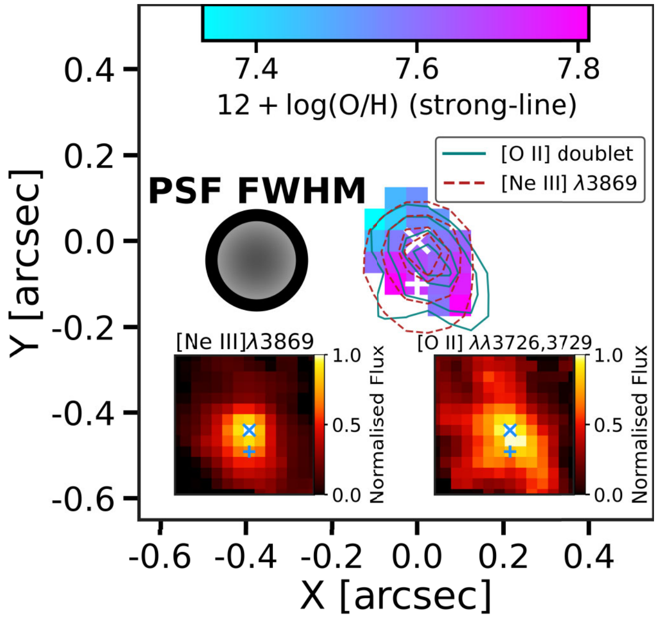

Figure 9. Metallicity map based on R_3-Ne_3O_2 line ratios (Section 4.4). Here, we only highlight the spaxels that have S/N > 5 for all lines involved and additionally S/N > 3 for [O III] λ4363 enabling a direct comparison to the direct method metallicity map (Fig. 5). We overplot the contours of the integrated fluxes of [O II] λλ3726, 3729 (teal, solid lines) and [Ne III] λ3869 (fire-brick, dashed lines). Both the contours and the inset panels show that [Ne III] has a more compact distribution, while [O II] is more extended. The '×' and '+' crosses in the inset panels are the centroids of peak Hγ (and [Ne III] λ3869) emission and of stellar continuum, respectively.

density of $n_H = 10^3$ cm^{-3}, similar to the average electron density reported by Abdurro'uf et al. (2024) for this system. However, no significant changes in the grid positions occur even if we instead choose $n_H = 10^2$ or 10^4 cm^{-3}. We assume a low dust-to-metal mass ratio of $\xi_d = 0.1$, suitable for $z > 10$ galaxies (A. Ferrara et al. 2025). The results are shown in Fig. 9, where we illustrate the positions of individual spaxels spectra on the chosen photoionization grid. To convert from $Z_\odot$ to oxygen abundance, we use $12 + \log(O/H) = 8.80 + \log(Z/Z_\odot)$, where 8.80 is the solar oxygen abundance computed by J. Gutkin et al. (2016) for $\xi_d = 0.1$. We obtain an excellent agreement between the results of the strong-line and direct-T_e methods, except for the southwestern region of the system. This is where line ratios show tentative evidence of photoionization influenced by other processes (Fig. 6b), in addition to star formation (such as AGN, shocks or diffuse ionized gas, DIG; the latter two will be discussed in Sections 5.2 and 5.3, respectively).

Indeed, previous studies have suggested that such abundance discrepancy factors between the two gas-phase metallicity calculation methods may be caused by ISM inhomogeneities (G. Stasińska et al. 2007; Y. Chen et al. 2023). We also note that, using multiple emission lines and assuming a stratified ISM with multiple density zones, numerical models indicate that the contribution of the dense gas component to [O III] λ4363 flux can increase the inferred total metallicity (e.g. A. Marconi et al. 2024). As a result, we provide a cautionary note regarding the interpretation of strong-line metallicities in the southwestern region.

4.5 Ionization parameter

For the ionization parameter, one standard approach is to use the diagnostic $O_{32} \equiv \log$ [O III] λ5007/ [O II] λλ3726, 3729 as these lines trace different ionization stages of the same atomic species (A. I. Díaz et al. 2000; L. J. Kewley & M. A. Dopita 2002; C. Papovich et al. 2022). [O III] λ5007 is unavailable in our spectra, despite our recovery of spectral data outside the nominal range of *G395M* grating. We therefore use Ne_3O_2 which closely tracks O_{32} and has the advantage that the wavelengths of these lines are close to each other, so their ratio is insensitive to dust reddening (T. Nagao, R. Maiolino & A. Marconi 2006; E. Pérez-Montero et al. 2007; E. M. Levesque & M. L. A. Richardson 2014; R. Maiolino & F. Mannucci 2019). To determine the ionization parameter, we use eq. (3) from J. Witstok et al. (2021, based on the original equation by A. I. Díaz et al. 2000 from single-star photoionization models).

With this standard approach, we obtain $\log U = -2.05 \pm 0.07$ for the full aperture spectrum and $\log U = -1.84 \pm 0.06$ for both the south-east and the north-west components, consistent with the result obtained by T. Y.-Y. Hsiao et al. (2024a). However, given the non-negligible spatial variations in gas-phase metallicity between different regions of the system (notably, between the SE-C and the NW-C), an alternative, more robust calculation of $\log U$ should take this effect into account. The most straightforward way to perform this calculation is to use the J. Gutkin et al. (2016) metallicity – ionization parameter photoionization grid (Fig. 8; also described in Section 4.4). By interpolating the measured positions of the data points corresponding to the full-aperture, SE-C, and NW-C spectra on the $R_3 - Ne_3O_2$ plane onto the grid, we obtain $\log U = -1.79 \pm 0.15$, -1.41 ± 0.19, and -1.47 ± 0.24 for the full-aperture, SE-C, and NW-C, respectively. The values calculated using this alternative method are higher than those determined using the standard, Ne_3O_2-based method that does not treat the metallicity dependence of this line ratio explicitly.

This implies that, in the case of a metal-poor ISM, the usual $Ne_3O_2 - \log U$ calibrations may substantially underestimate the ionization state. The calculated $\log U$ values are also higher than those of other SFGs at $3.5 < z < 10$ (L. Christensen et al. 2012; P. Troncoso et al. 2014; A. E. Shapley et al. 2017; C. Marconcini et al. 2024; B. Rodríguez Del Pino et al. 2024; M. J. Hayes et al. 2025; E. Parlanti et al. 2025b), suggesting a more intense radiation field. Our values are instead similar to other $z > 10$ galaxies such as GHZ2 (M. Castellano et al. 2024; J. A. Zavala et al. 2025) and GN-z11 (A. J. Bunker et al. 2023). On spatially resolved scales, Fig. 5(b) shows a relatively uniform Ne_3O_2 (and, by extrapolation, $\log U$) in the central regions of MACS0647-JD1, with a radial decrease of 0.33 ± 0.14 dex from the centre of the system towards its outer regions, with substantially lower ionization in the southwestern region, a feature possibly indicating ionization stratification, which we discuss in greater detail in Section 5.1.

5 THE NATURE OF THE MACS0647-JD SYSTEM

5.1 Emission-line spatial distribution

To characterize the morphology of the ISM within the MACS0647-JD1 system, we first identify the brightest spaxel in the emission-line maps of Hγ and [Ne III] λ3869. This spaxel is shifted by two spaxels (corresponding to a physical, delensed distance of ~ 150 pc, as shown in Fig. 2) relative to the centroid of the synthetic *F444W* image obtained by convolving the datacube with the response function of the NIRCam/*F444W* bandpass. Such a shift could arise from differential dust attenuation between the emission lines and the stellar continuum. However, MACS0647-JD is dust poor (as shown in Section 4.3 and by T. Y.-Y. Hsiao et al. 2024a), making this possibility unlikely. Thus, the observed offset likely implies a different spatial distribution of the line-emitting gas relative to the stars. Since the instantaneous SFR directly determines the strength of the Balmer lines (R. C. Kennicutt & N. J. Evans 2012), it means that the central region between the two stellar clumps (Fig. 2b) hosts the most intense recent star formation activity, while the two stellar components are dominated by older stellar populations. This could favour a merger scenario for this system, in agreement with the findings of Q. Duan et al. (2026b) and D. Puskás et al. (2025a), who report that, on average, high-redshift mergers trigger short-lived star formation enhancements if the components become separated by a proper distance of less than 20 kpc.

There is a striking difference between the spatial distributions of the [O II] $\lambda\lambda$3726, 3729 and [Ne III] λ3869 emission. The latter is a representative tracer of the high-ionization compact central region of the system (with very similar morphologies revealed by both Balmer recombination lines and [O III] λ4363, all of which are shown in Appendix A). In contrast, the [O II] $\lambda\lambda$3726, 3729 emission is both clumpier and more spatially extended, primarily tracing the low ionization gas in the system. Since we observe that $\log(Ne_3O_2) > 0$ even in the outskirts, the most plausible explanation is a classical, inside–out stratification of the system, although we cannot completely rule out more exotic scenarios such as the presence of DIG (e.g. K. Zhang et al. 2017), which typically boosts [O II] $\lambda\lambda$3726, 3729 emission (D. A. Hunter & J. S. Gallagher III 1990; R. C. Kennicutt 1998) and metal lines strength (P. Garg et al. 2024; W. McClymont et al. 2024; A. Clarendon, A. Strom & C. von Raesfeld 2025). A recent NIRSpec/IFU study by T. A. Hutchison et al. (2025) tentatively identified DIG in a highly lensed $z \sim 5$ massive post-starburst galaxy. However, while [O II] $\lambda\lambda$3726, 3729 emission truly appears enhanced relative to hydrogen lines in the southern and southwestern regions of our target (compared to the central regions), T. Y.-Y. Hsiao et al. (2025) report non-detections of [N II] λ6548 and [N II] λ6583 (these lines are expected to be prominent in regions with DIG) in the MIRI spectra. This challenges the interpretation that DIG is present in the southern-southwestern region of the MACS0647-JD1 system. Of course, at $z > 10$, intrinsically low N/O abundance ratios could also explain the undetected [N II] doublet in the extended region, given that N/O-enhanced systems tend to be very compact (e.g. X. Ji et al. 2026).

5.2 Shock-driven photoionization modelling

Given the tentative position of the spaxels in the southwestern region of the system in the AGN-dominated region of the G. Mazzolari et al. (2024) diagnostic diagram, as well as the subtle discrepancy between the gas-phase metallicities calculated using the direct-T_e and the strong-line methods, we test the possibility that shocks may have a significant contribution to the photoionization. We use an approach similar to that of F. D'Eugenio et al. (2025c), who report shock-driven photoionization in an SFG at $z \sim 4.6$. We use the shock models from the 3MdB data base.[4] The grids are computed using the MAPPINGS V code (R. S. Sutherland & M. A. Dopita 2017). We tested both shock only and shock with precursor models (M. G. Allen et al. 2008; A. Alarie & C. Morisset 2019) spanning a large parameter space (the BnZv space): magnetic field 10^{-4} μG $< B < 10$ μG, shock velocity 100 km s^{-1} $< v <$ 1000 km s^{-1}, pre-shock (upstream) density 1 cm^{-3} $< n_{\rm sh} <$ 10 000 cm^{-3} and metallicity $10^{-4} < Z < 0.04$. The metallicities are converted to oxygen abundance values assuming $Z_\odot = 0.01524$ and $12 + \log(O/H)_\odot = 8.8$ (using the same chemical abundances from J. Gutkin et al. 2016 as used by A. Alarie & C. Morisset 2019 in the shock grid calculations and adopting a dust depletion $\xi_d = 0.1$, similar to Section 4.4). As before, we choose the $C/O = 0.72\,(C/O)_\odot$ photoionization parameters from J. Gutkin et al. (2016).

In our particular case, we select a fixed magnetic field strength of $B = 10$ μG for all models displayed in Fig. 10. This value is comparable to the magnetic field in the solar neighbourhood (2 − 25 μG; J. P. Vallee 2022). However, there is plausible evidence that the galactic magnetic fields are likely larger in starburst galaxies (50 − 100 μG; R. Beck 2015), and at earlier cosmic times (A. M. Wolfe et al. 2008). Because 10 μG is the highest value available in the computed shock grids, we regard this value as the most sensible choice. The diagnostic line ratios considered here (O_3Hg and Ne_3O_2) are only weakly sensitive to the magnetic field strength over the range of parameter space probed by our data. In particular, magnetic-field-dependent effects become significant only at very low O_3Hg ratios, $\log([O\,III]\,\lambda4363\,/\,H\gamma) < -1.5$, where model tracks corresponding to different magnetic fields diverge.

We explore shock model grids with pre-shock densities, $n_{\rm sh}$ = 100, 1000, and 10 000 cm^{-3}. Models with $n_{\rm sh} \lesssim 100$ cm^{-3} are unable to reproduce the observed O_3Hg and Ne_3O_2 measurements in any configuration, so they are strongly disfavoured. For $n_{\rm sh} = 10^3 - 10^4$ cm^{-3}, shock-plus-precursor grids (Figs 10e and f) intersect the data only for parameter combinations that imply oxygen abundances of $12 + \log(O/H) \sim 8.2 - 8.4$, exceeding the metallicities inferred from spaxel or clump aperture spectra

[4] https://sites.google.com/site/mexicanmillionmodels/

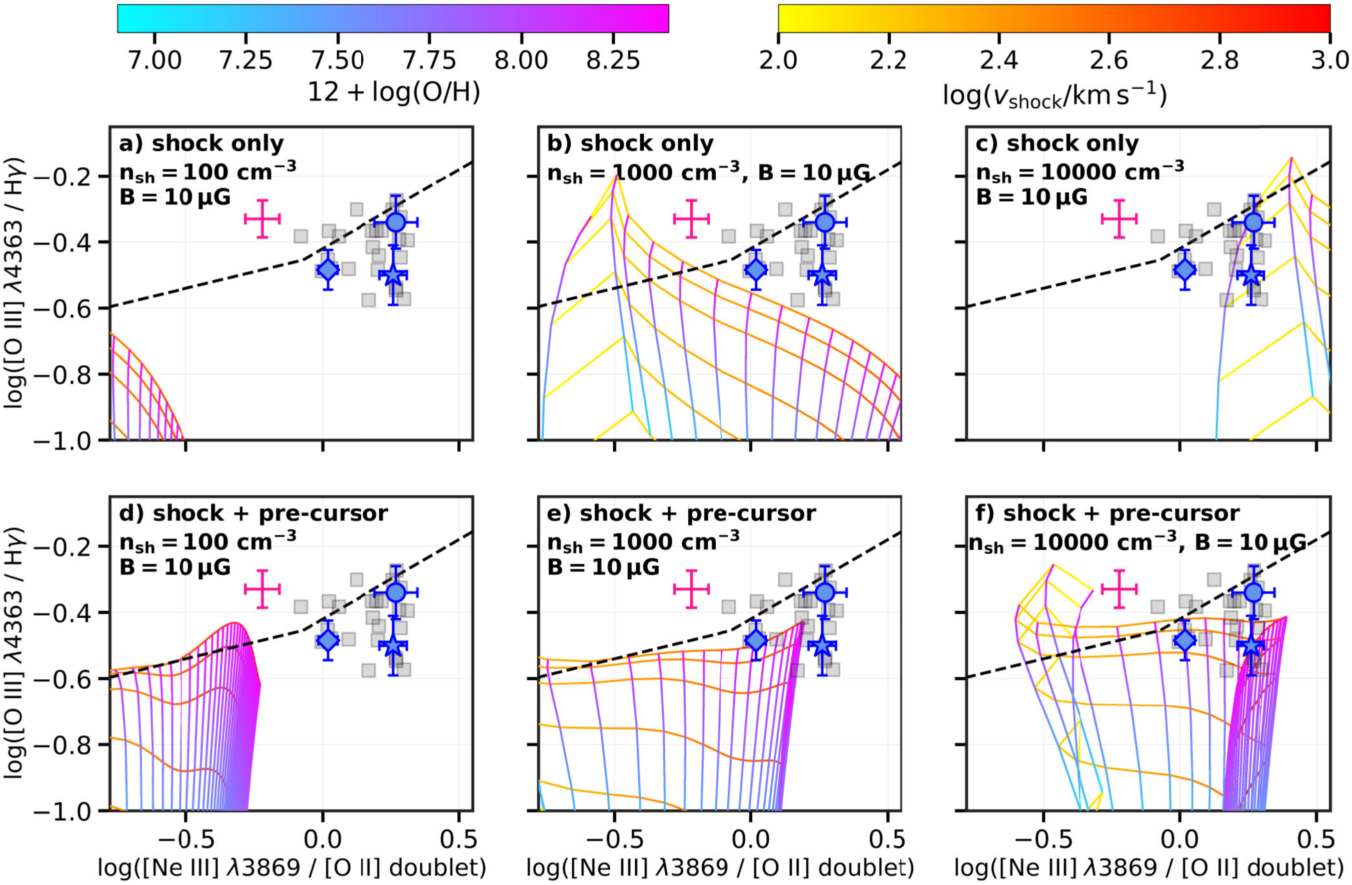

Figure 10. In this figure, we illustrate the various shock models overlaid on the G. Mazzolari et al. (2024) diagnostic diagram, in order to compare with our data points. Individual spaxels are marked with squares (with the standalone error bars showing their median uncertainties), whereas the large star, diamond and circle symbols have similar meanings to Fig. 6(a): the diamond represents the full aperture, the star is the SE-C, and the circle is the NW-C. The black, dashed line is the demarcation between the AGN-dominated regime and the regions where SF and AGN have similar contributions to photoionization (SF or AGN regime). We display a number of shock and shock + precursor grids computed using MAPPINGS V (R. S. Sutherland & M. A. Dopita 2017) at fixed pre-shock density, $n_{\rm sh}$, fixed magnetic field, $B = 10\ \mu$G and varying metallicity $7 < 12 + \log(\mathrm{O/H}) < 8.4$ and shock velocity $2 < \log\left(v_{\rm shock}\,/\,\mathrm{km\ s^{-1}}\right) < 3$. Our observations can only be reproduced with either high metallicities or high pre-shock densities, which, although not completely ruled out locally, are difficult to reconcile with the gas-phase metallicities (Fig. 5c) and electron densities inferred by Abdurro'uf et al. (2024) for our system.

$(12 + \log(\mathrm{O/H}) \sim 7.2 - 8.0$ using either the direct or the strong-line method). It is generally true that the metallicities calculated with the direct method might be biased low if shocks are present and not accounted for. This is because shocks alter the ionization structure of the ISM and can create large temperature variations on small spatial scales. As a result, the electron temperature and oxygen abundance may be decoupled, causing metallicities to be underestimated in shock-heated regions. However, the shock grid displayed in Fig. 10(e) further requires high velocity shocks ($\sim 500 - 1000$ km s^{-1}) to match our data. Such velocities are substantially larger than the characteristic ionized gas kinematic widths in our system (FWHM $\sim 100 - 350$ km s^{-1}). Additionally, our spectral fits show no statistical requirement for an additional broader component, together suggesting that these shock-plus-precursor models are unlikely to dominate over star-formation-driven photoionization on large scales, but they may be important locally.

A shock-only model with $B = 10\ \mu$G and $n_{\rm sh} = 10^4$ cm^{-3} (Fig. 10c) can reproduce the observed line ratios for the SE-C and NW-C apertures at lower metallicities and lower shock velocities than the shock-plus-precursor cases. However, such a model requires an upstream density of 10^4 cm^{-3}. Moreover, shocks compress the gas by at least a factor of four in the strong adiabatic shock limit (and potentially more if radiative), implying post-shock densities $\gtrsim 4 \times 10^4$ cm^{-3}. While these required densities are at least one order of magnitude above the average electron density of $\log\left(n_{\rm e}/\mathrm{cm^{-3}}\right) = 3.3^{+0.7}_{-0.6}$, derived from the full-aperture spectrum of the MACS0647-JD1 image (Abdurro'uf et al. 2024), this direct comparison is not fully conclusive for ruling out shock-driven photoionization processes. The reported electron density was obtained by Abdurro'uf et al. (2024) by spectrally resolving the [O II] λ3726, 3729 doublet with high-resolution *JWST* spectroscopy. PYNEB predicts critical densities of ~ 1500 and ~ 5000 cm^{-3} (assuming an electron temperature of 1.9×10^4 K, similar to the one derived from the full aperture spectrum) for [O II] λ3729 (first upper level) and [O II] λ3726 (second upper level), respectively. These values are in agreement with those obtained by W. Wang et al. (2004). As a result, this doublet primarily traces low-ionization and lower density phases of the ISM. In a multizone ISM, the [O II]-based density may not fully capture denser gas that might produce the bulk of [O III] λ4363 ($n_{\rm crit} \sim 3 \times 10^7$ cm^{-3}; B. Moreschini et al.

2026) emission or shocks. Recent observational and ISM modelling studies have further revealed that metallicities inferred under a low-density ISM assumption may be underestimated (A. Marconi et al. 2024; Y. Harikane et al. 2025; Z. Martinez et al. 2025; B. Moreschini et al. 2026). This is because auroral lines such as [O III] λ4363, commonly used in direct-T_e method calculations, typically probe higher density regions (T. Jones et al. 2020; S. Yang & A. Lidz 2020; S. Yang, A. Lidz & G. Popping 2021; Y. Nakazato, N. Yoshida & D. Ceverino 2023). In high-density regimes, collisional de-excitation and radiative decays have comparable contributions to de-populating the atomic upper levels associated with the key emission lines, which could bias our estimated abundances. Invoking a substantial fraction of the ionized gas mass with a density of $\sim 10^5 - 10^6\,\mathrm{cm^{-3}}$ (to accommodate the high pre-shock densities required to match the observed emission-line ratios; Fig. 10) would be difficult to reconcile with a starburst-dominated system exhibiting only marginal and localized evidence for non-SF processes. A complete picture would require high-resolution *JWST* IFU observations of the system using the *G235H* or *G395H* gratings. Such observations would provide spatially resolved maps of both low- and high-density gas (by spectrally resolving the [O II] λ3726, 3729 and the far-ultraviolet C III]$\lambda\lambda$1907, 1909 doublets, respectively).

Furthermore, as a simplified, illustrative approach, under the assumption that shocks are the main excitation mechanism of the ISM in MACS0647-JD1, we can estimate the average photoionization mass rate associated with this process. If shocks rather than star formation dominate the emission-line production, it means that at least half of the [O III] λ5007 flux (total of $(2.24 \pm 0.52) \times 10^{-17}\,\mathrm{erg\,s^{-1}\,cm^{-2}}$) would arise from the shock line component. Taking into account the luminosity distance and the magnification of the system, this would imply $L_{[\mathrm{O\,III}]\lambda5007,\,\mathrm{shocks}} \gtrsim 2 \times 10^{42}\,\mathrm{erg\,s^{-1}}$. According to the first equation from A. Laor (1998), and adopting a typical maximum shock velocity of $v \sim 1000\,\mathrm{km\,s^{-1}}$ (similar to the maximum value within the shock grids from the 3MdB data base), we would obtain $M_{\mathrm{shocked\,gas}} \gtrsim 100\,\mathrm{M_\odot\,yr^{-1}}$. This value is significantly larger than the inferred Hγ-based SFR of $\sim 5.5 \pm 1.0\,\mathrm{M_\odot\,yr^{-1}}$, consistent with our starting assumption. If the gas mass in the system is comparable to the stellar mass (see the discussion in Section 5.5), such a high rate of shock-driven photoionization of the cold gas would imply that this reservoir would be consumed on $\lesssim 1 - 5$ Myr time-scales, shorter than the stellar ages of $\sim 20 - 30$ Myr of the two clumps derived from SED fitting. Overall, while we cannot firmly rule out shocks affecting the structure and ISM properties of MACS0647-JD1, the existing observations favour a starburst-dominated ISM.

5.3 Spatially resolved properties of the ISM gas

Based on our methods for calculating the strong-line metallicity (discussed in Section 4.4), we obtain the map shown in Fig. 9. We applied similar spatial cut of the map in order to facilitate the comparison with the direct metallicity map (Fig. 5c). We find that our results are consistent between these methods. Both the direct-T_e and the strong-line methods reveal that the SE-C is more enriched than both the NW-C and the turbulent, metal-poor gas located in the NE region (NE-R) of the system (i.e. between the two clumps).

To provide quantitative evidence of the different nature of the ISM at various locations, we divide the observed system within the field of view in four regions, as shown in Fig. 2: the NW-C and SE-C, together with the NE-R and SW-R. We illustrate the resulting direct-T_e and strong-line metallicities from the integrated spectra of these four apertures (obtained by adding the spaxels within each aperture) in Fig. 12. We find that, for each aperture, the two methods of calculating the metallicity give consistent results. Moreover, Fig. 12 shows that, although some non-negligible spaxel-to-spaxel variations may occur in our maps, our conclusion that the SE-C is more metal-rich than its surrounding environment is statistically robust.

Fig. 5(a), (c), and (d) reveal spatial variations in gas kinematics, excitation, and chemical properties across the system, suggesting possible connections between gas velocity dispersion, excitation-sensitive line ratios (particularly O_3Hg), and gas-phase metallicity on spatially resolved scales. We quantify these trends by testing for spaxel-scale correlations between gas velocity dispersion (FWHM) and ISM properties. We find a significant anticorrelation between FWHM and the O_3Hg line ratio (with a p-value of 1.2×10^{-3} and a Spearman correlation coefficient $\rho \sim -0.62$; Fig. 11a). While this correlation is intriguing, its physical origin is difficult to pinpoint because the [O III] λ4363/Hγ ratio depends simultaneously on multiple ISM properties, including metallicity, electron temperature, ionization parameter, and the local SFR. We find only a marginal anticorrelation between FWHM and metallicity, and a tentative positive correlation between FWHM and electron temperature (as shown in Figs 11b and c). Our analysis does not find any correlation between FWHM and Ne_3O_2 ($p \sim 0.38$; Spearman correlation coefficient of $\rho \sim -0.12$), although central spaxels tend to have both high O_3Hg and high Ne_3O_2 ratios. Similar to our calculation in Section 4.5 for the integrated-aperture spectrum, we compute the ionization parameters for the spectra of all individual spaxels, based on the J. Gutkin et al. (2016) photoionization grid. We find only a weak, statistically insignificant correlation between FWHM and $\log U$ of individual spaxels ($p \sim 0.08$; $\rho \sim +0.24$). Remarkably, we also obtain a correlation of higher significance between FWHM and the star formation burstiness ($\mathrm{SFR_{10}/SFR_{100}}$), with $\rho \sim +0.39$; $p \sim 10^{-3}$. We note that, in this case, the total number of spaxels considered is larger than for the anticorrelation reported between FWHM and O_3Hg, and the tentative FWHM $-$ T_e and FWHM–metallicity correlations. This is because in the latter case, we take into account all spaxels with $\mathrm{S/N_{H\gamma}} > 5$, whereas in the former case, we are restricted to the central region of the system for which we imposed $\mathrm{S/N}_{[\mathrm{O\,III}]\lambda4363} > 3$ for a statistically significant detection of this auroral line. We caution that the reported Spearman coefficients and p-values are based on median estimates using face-value measurements in the individual spaxels considered for each pair of physical parameters or observables. A bootstrap analysis accounting for per-spaxel uncertainties yields p-values exceeding 0.05 for the FWHM–T_e and FWHM–metallicity relations, indicating that these trends are not robust. Only the correlation between FWHM and O_3Hg remains significant, with an 84th-percentile p-value of 0.028.

The differing strengths of these correlations likely reflect the fact that O_3Hg is a direct and unbiased observable that is sensitive to both the local excitation and thermal conditions of the ionized gas in the ISM, and also to the local instantaneous SFR. By contrast, the electron temperature and the inferred metallicity are derived quantities subject to additional assumptions and associated systematic uncertainties. The most important of these include a secondary dependence on the ionization parameter, the possibility of a multizone ISM, as well as possible uncertain dust corrections in calculations of metallicities and electron temper-

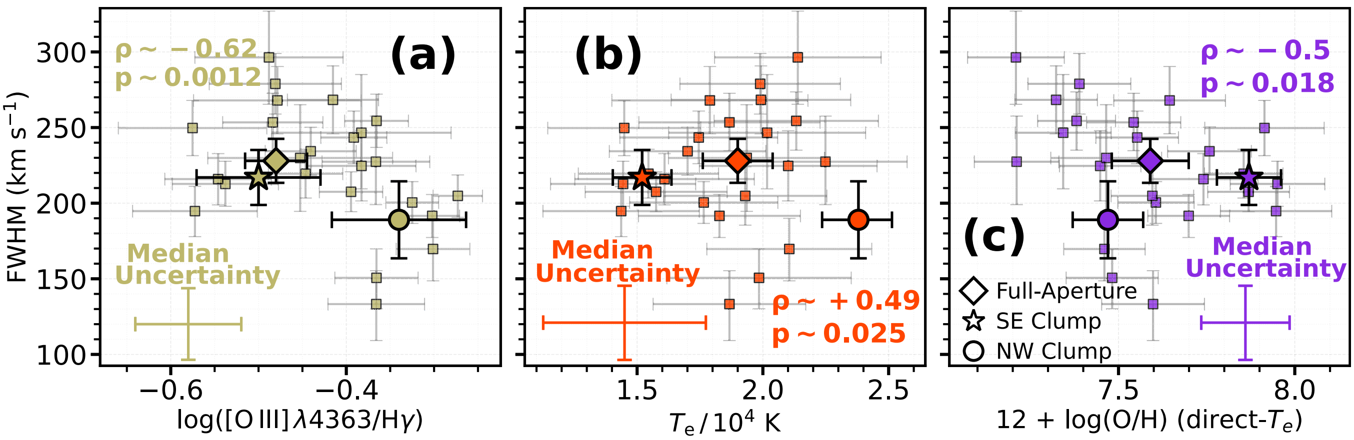

Figure 11. This figure shows the variation of gas velocity dispersion (FWHM) as a function of O$_3$Hg line ratio (a), electron temperature (b) or gas-phase metallicity calculated using the direct method (c). As before, we only show the spaxels with $S/N_{[O\,III]\lambda4363} > 3$, but we also show the values corresponding to the SE-C and NW-C and for the full-aperture spectra. We display the individual and the typical median uncertainties for the per-spaxel measurements. The bootstrapped median Spearman correlation coefficient ρ and the p-value are reported for the set of correlations considered.

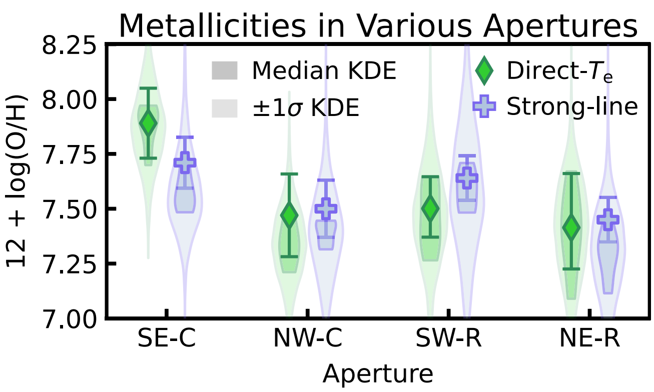

Figure 12. This figure shows the calculated gas-phase metallicities (using both the direct-T_e and the strong-line methods) and the uncertainties for the spectra of the four apertures identified in Fig. 2(b). For each aperture and method, violin plots illustrate the ranges of metallicities of spaxels within the said aperture. Darker-shade violins show the kernel density estimate (KDE) of median metallicities, while lighter-shaded violins include $\pm 1\sigma$ spaxel-level uncertainties.

atures. Importantly, a locally elevated temperature of the O^{++} gas may not necessarily imply a higher [O III] $\lambda4363$ / Hγ ratio. While the effective Hγ recombination rate has a weak inverse dependence on electron temperature, this effect can be easily outweighed by spatial variations in electron and ion densities or gas filling factor, particularly in a complex, multizone ISM. The gas FWHM traces emission-line broadening due to both thermal and non-thermal processes. The presence of dynamically turbulent and hot gas (as shown in Figs 5d and 7b) between the clumps may indicate enhanced energy injection into the ISM. This may arise from localized shocks (see the discussion in Section 5.2 for arguments disfavouring large-scale shock-driven photoionization), or from a combination of turbulent star formation-driven feedback and complex gravitational interactions between the clumps and the surrounding metal-poor gas. Our observational findings agree with recent theoretical models, which posit that turbulent gas in low-mass bursty galaxies at high redshift, being highly dynamically unstable, favours clumpy star formation, and an ISM with large density and temperature variations, even on relatively small spatial scales (G. Sun, C.-A. Faucher-Giguère & J. Stern 2026), providing a possible explanation for why there is a statistically significant correlation between FWHM and star formation burstiness.

Our results disagree with results from the local Universe and lower redshift studies, which find positive correlations between gas-phase metallicity and (stellar) velocity dispersion for massive, evolved galaxies (e.g. H. Li et al. 2018; M. Cappellari 2023). Such a positive correlation is also seen in individual galaxies within the SPT0311−58 protocluster at $z \sim 6.9$ (S. Arribas et al. 2024). The possible anticorrelation observed in the case of MACS0647-JD is likely not the result of secular, interconnected processes shaping the co-evolution of various galaxy properties. Such processes have not yet been established in low-mass systems at $z > 10$. Instead, our findings suggest that our target is observed in an early, short-lived evolutionary phase.

5.4 Spatially resolved stellar populations: bursty star formation in the northeastern region of the system

We compute the burstiness of star formation on spaxel-by-spaxel scales using the SFR averaged over the last 100 Myr in lookback time (SFR$_{100}$ from our PROSPECTOR SED fits) as a probe of the long-time-scale SFR. For instantaneous or short-time-scale SFR, we use two alternative tracers: (i) SFR$_{10}$ (similar to SFR$_{100}$ but it probes only the last 10 Myr in lookback time; this is also computed by PROSPECTOR); and (ii) SFR$_{H\gamma}$ inferred from the Hγ integrated line flux. To estimate SFR$_{H\gamma}$, we first correct the Hγ fluxes of each spaxel based on the observed Hβ/Hγ Balmer decrement in that spaxel (we assume no dust correction in the cases where the Hβ/Hγ ratio from the spectrum is lower than the case-B value of 2.105). We then assume an intrinsic, case-B Hα/Hγ = 5.79 ratio, valid for an electron temperature $T_e \sim 20\,000$ K (B. Groves et al. 2012) and we adapt the relation between Hα intrinsic luminosity and SFR from eq. (12) of R. C. Kennicutt & N. J. Evans (2012) as follows:

$$\log \mathrm{SFR}_{\mathrm{H}\gamma}\,(\mathrm{M_\odot\,yr^{-1}}) = \log \mathrm{L}_{\mathrm{H}\gamma}\,(\mathrm{erg\,s^{-1}}) - 40.5 - \log\mu - 0.3. \quad (5)$$

Here, for delensing, we assume a lensing magnification of $\mu = 8 \pm 1$ (B. M. Y. Chan et al. 2017). However, the SFR–Hα equation derived by R. C. Kennicutt & N. J. Evans (2012) is calibrated in the local Universe, assuming a solar metallicity and a D. Calzetti et al. (2000) dust attenuation law. At higher redshifts, galaxies typically have different properties from local targets, so a more suitable set of assumptions is a different dust attenuation law and a lower metallicity. N. A. Reddy et al. (2022) and A. E. Shapley et al. (2023) showed that the correction term is around −0.3 dex if we instead assume a Small Magellanic Cloud dust attenuation law and a metallicity of 0.27 $Z_\odot$.

We show our results in Figs 13(a) and (b). Both panels indicate a significant enhancement of recent star formation in the NE-R, the same location where the gas is both more turbulent (Fig. 5d) and metal-poor (Fig. 5c). By contrast, the more massive, more metal-enriched SE-C does not undergo a noticeable starburst episode within the time-scales probed. As shown in Fig. 13(b), we find only moderate burstiness in the two clumps (more pronounced for the NW-C). Fig. 13(c) confirms the more massive nature of the two clumps compared to the surrounding regions. The stellar mass densities of the spaxels in the NE-R are typically ∼ 1 dex below the values within the two clumps, which implies that this region may be associated with a metal-poor gas inflow. Another plausible scenario is that this region contains gas stripped from the NW-C by gravitational interactions with the massive SE-C. Indeed, the metallicities of NE-R and NW-C are consistent within the uncertainties as shown in Fig. 12.

More puzzlingly, the SW-R of the system, which is intrinsically fainter than either of the clumps, appears to be substantially more massive than the bursty, low-M_* NE-R. In addition, $\mathrm{SFR}_{\mathrm{H}\gamma}$ indicates negligible star formation enhancement (Fig. 13a). When recent star formation is instead probed via SFR_{10}, a starburst effect is observed in the SW-R, although it is less intense than in the NE-R. Physically, the SW-R could represent gas and stars that originated in the SE-C, but were redistributed during a merger event.

5.5 Merging galaxies or clumps in a disc?

The observed properties of MACS0647-JD1 allow, in principle, two broad interpretations: either the system represents a gas-rich rotating disc hosting multiple clumps, or it is caught during an early-stage merger between two distinct components. Disc galaxies are generally characterized by a ratio of ionized gas velocity to velocity dispersion of $V_{\mathrm{gas}}/\sigma \gtrsim 1$ and by ordered rotation on spatially resolved scales (N. M. Förster Schreiber & S. Wuyts 2020; A. L. Danhaive et al. 2025). In Appendix C, we show that the observed rotational pattern in the velocity field of the MACS0647-JD1 system may be dominated by instrumental systematics, making it difficult to recover the intrinsic velocity field. One reason why we cannot firmly dismiss the hypothesis of a real rotating structure is the fact that the rotational gradient is spatially more extended than the FWHM of the PSF (the latter being ∼ 4.4 spatial pixels). In addition, as we argue in Appendix C, the amplitude of the artificial rotation pattern produced by the slit-width effect (described in Y. Isobe et al. 2023a and Appendix C) is noticeably smaller (2.6 times) than the observed velocity gradient in our data. It is, however, crucial to note that we only provide a simplified calculation that illustrates that the slit-width effect could potentially mimic a rotational pattern in *JWST*/NIRSpec IFU data. Disentangling instrumental effects from genuine galaxy kinematics would require additional IFU observations obtained at a position angle rotated by 90° relative to the current setup (Fig. C2a).

In this section, we argue that the morphological, chemical, and kinematic properties of this system are more naturally explained by a gas-rich merger between the NW-C and the SE-C. First and foremost, the two main components exhibit markedly different gas-phase metallicities (see Section 5.3), with the SE-C being significantly more enriched than both the NW-C and the surrounding gas. Using the values in Table 1, we obtain a metallicity difference of 0.42 ± 0.18 dex (using direct-method metallicities; or 0.22 ± 0.12 dex using the metallicities derived based on the strong-line method) between the two main components of the system. Such metallicity contrasts over short projected physical scales (∼ 300 pc in the source frame, assuming a magnification of $\mu \sim 8$) are difficult to reconcile with *in-situ* clump formation within a single disc, where clumps primarily form from the existing ISM gas reservoir. While several studies have revealed metallicity inhomogeneities in proto-disc systems at $z > 6$ (S. Arribas et al. 2024; G. Venturi et al. 2024; L. R. Ivey et al. 2026b), the reported metallicity gradients are $\left|\nabla_r \log(\mathrm{O/H})\right| \lesssim 0.2\,\mathrm{dex\,kpc^{-1}}$. The amplitude of the variations we measure in the MACS0647-JD system suggests that additional processes beyond simple *in-situ* fragmentation (such as external fresh gas accretion or mergers) may be involved.

Second, the highest gas velocity dispersions are observed outside the two massive clumps (Fig. 5d) and are anticorrelated with excitation-sensitive line ratios (Fig. 11a). This suggests that turbulence is not primarily driven by star formation feedback, as expected in clumpy discs, but by gravitational interactions possibly leading to a large-scale circulation of the gas, consistent with a merger scenario. The observation of this dynamically hot gas in the regions outside the main components is facilitated by the lack of strong stellar sources in these locations, allowing the emission lines to probe large path lengths along the line of sight and therefore trace large-scale gas motions. In addition, the star formation burstiness maps show a clear asymmetry (Fig. 13): the most intense enhancement of recent star formation is in the NE-R, cospatial with confidently identified metal-poor, highly turbulent gas.

Third, the centroid of nebular emission is offset from the stellar continuum peak by at least two spatial pixels (∼ 0.1 arcsec, measured using the Hγ emission map; see Fig. 2). The spatial offset is larger if we consider, for instance, Hβ, Hδ, or [Ne III] λ3869 centroids. While instrument systematics can sometimes create an artificial shift of the centroid of point sources as a function of wavelength, the magnitude of this effect is too small (∼ 0.02 arcsec; T. Beck 2025) to justify the different spatial distributions of stellar continuum and emission lines. In a clumpy disc, the most intense line emission is generally cospatial with the dominant stellar clumps (e.g. A. B. Romeo & K. M. Mogotsi 2017), whereas star formation between stellar components is more naturally explained by merger-driven gas instability.

Although an accurate estimate of the gas mass in the system requires the completion of the existing allocated *NOEMA* observations, we can provide a crude estimate using a method similar to K. Nakajima et al. (2026). The angular separation between the two clumps is approximately 0.15 arcsec (as shown in Figs 2a and 13c), corresponding to ∼ 220 pc in the source plane. As a result, given our delensed value of the $\mathrm{SFR}_{\mathrm{H}\gamma}$ estimated for the full-aperture spectrum, $\mathrm{SFR}_{\mathrm{H}\gamma} = 5.5 \pm 1.0\,\mathrm{M_\odot\,yr^{-1}}$ (Table 1), and assuming an approximate radius of ∼ 200 ± 50 pc for the gas reservoir in the inter-clump region, we obtained an SFR density of $\log\left(\Sigma_{\mathrm{SFR}_{\mathrm{H}\gamma}}/\mathrm{M_\odot\,yr^{-1}\,kpc^{-2}}\right) = 1.35 \pm 0.30$. We use eq. (2) from N. Bouché et al. (2007) to estimate the gas mass surface density.

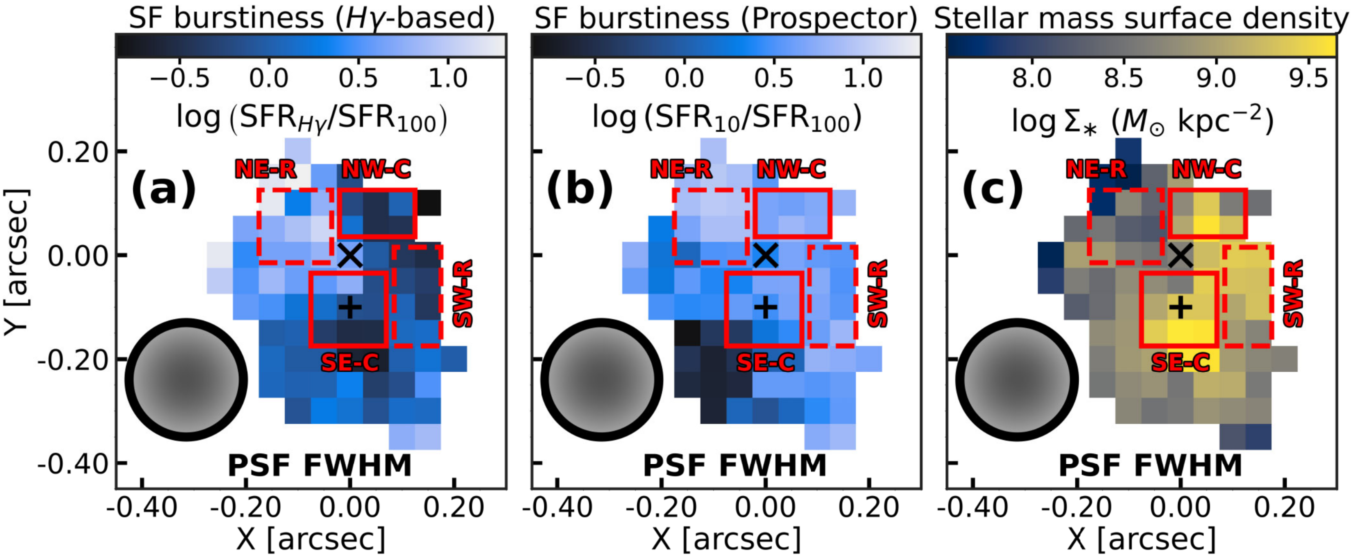

Figure 13. In this figure, we display the spatially resolved star formation burstiness in MACS0647-JD1 system. The burstiness probes the recent versus prolonged star formation activity in our target, and is defined in two alternative ways: $SFR_{H\gamma}/SFR_{100}$ (a) and SFR_{10}/SFR_{100} (b). The rectangles are the apertures corresponding to the two clumps (SE and NW, as identified from NIRCam *F444W* imaging; see Fig. 2). Both maps consistently show a remarkable recent star formation enhancement in the NE-R and a less bursty SFH in the region of the more massive SE-C. (c) Shows the stellar mass density map of this system and confirms the more massive nature of the two clumps, compared to other regions. On all panels, we only show the spaxels with a S/N > 5 detection of Hγ from our analysis of NIRSpec/IFU data. We also show the PSF size in all panels, together with the centroid of stellar continuum ('+' cross) and of the Hγ emission-line map ('×' cross).

In this equation, $\Sigma_{\rm SFR} \propto \Sigma_{\rm gas}^{1.71\pm0.05}$ and the power-law index of 1.71 ± 0.05 is significantly larger than the 1.4 ± 0.15 value given in R. C. Kennicutt (1998). This substantial difference arises from collisionally enhanced star formation efficiency in high-density gas ($\sim 1000\,{\rm cm^{-3}}$), a regime which is more commonly observed in the ISM of high-redshift galaxies. With our previous value of $\log \Sigma_{\rm SFR_{H\gamma}}$, we obtain $\log\left(\Sigma_{\rm gas}\,/\,{\rm M_\odot\ pc^{-2}}\right) = 3.15 \pm 0.20$, implying $\log\left(M_{\rm gas}\,/\,{\rm M_\odot}\right) = 8.6 \pm 0.3$. This indicates that the gas mass in MACS0647-JD1 is likely larger than the stellar mass within the SE-C and NW-C.

If the system is a rotating disc, we can estimate its dynamical mass using the following equation (adapted from M. Cappellari et al. 2006):

$$M_{\rm dyn} \approx \frac{5R_{\rm eff}\,\sigma_*^2}{G}. \quad (6)$$

We assume an effective radius $R_{\rm eff} = 70 \pm 24$ pc (T. Y.-Y. Hsiao et al. 2024a) and estimate the stellar velocity dispersion from the gas velocity dispersion, $\sigma_{\rm gas} = {\rm FWHM_{gas}}\,/\,2.355 = 97 \pm 8\ {\rm km\ s^{-1}}$ from the full-aperture spectrum. Adopting the empirical relation $\sigma_* \approx 1.26 \times \sigma_{\rm gas}$ (R. Bezanson et al. 2018), we obtain $\sigma_* = 122 \pm 10\ {\rm km\ s^{-1}}$ and therefore $\log(M_{\rm dyn}/{\rm M_\odot}) = 9.1 \pm 0.5$. The quoted uncertainty accounts for the standard scatter of the virial mass estimator equation and the systematics associated with choosing a factor of 5 in equation (6), instead of using eq. (7) from A. van der Wel et al. (2022). The latter equation accounts more accurately for variations due to the object's axial ratio and Sérsic index. However, given the two-clump morphology of our target (Fig. 2b), a simple single Sérsic profile fit to the *F444W* image of MACS0647-JD1 would not be suitable. This caveat prevents us from applying morphology-dependent virial corrections such as those discussed in A. van der Wel et al. (2022).

The estimated dynamical mass of the system is statistically consistent (within the 1σ uncertainties) with the combined mass of the stars (see Table 1) and gas. However, this comparison does not provide a decisive diagnostic of the dynamical state of the system. The dark matter (DM) mass, on the other hand, is even more difficult to accurately constrain at such high redshifts. Galaxies at $z > 4$ and $\log(M_*/{\rm M_\odot}) < 9$ are expected to be strongly DM dominated, as revealed by recent *JWST* spectroscopic observations (A. de Graaff et al. 2024a; A. L. Danhaive et al. 2026a) and simulations (A. de Graaff, A. Pillepich & H.-W. Rix 2024b; W. McClymont et al. 2026). We can provide a simple estimate of the DM mass in the central region between the two clumps as follows. The total stellar mass of the two clumps is $\log(M_{*,\,\rm NW+SE}/{\rm M_\odot}) = 7.94 \pm 0.09$. We assume that the DM density follows the classical NFW profile (with the inner slope $\gamma = -1$) satisfying the equation (J. F. Navarro, C. S. Frenk & S. D. M. White 1996; J. S. B. Wyithe, E. L. Turner & D. N. Spergel 2001):

$$\rho_{\rm DM}(r) \propto \frac{1}{(r/r_{\rm b})^{-\gamma} \cdot (1 + r/r_{\rm b})^{\,3+\gamma}}. \quad (7)$$

Here, $r_{\rm b}$ is the so-called break radius of the DM halo of MACS0647-JD1. Using the stellar mass–halo mass (SMHM) relation from P. Behroozi et al. (2019), we obtain a virial halo mass of $\log(M_h/{\rm M_\odot}) \approx 10.5 \pm 0.3$. Here, the quoted uncertainty combines the intrinsic scatter of the SMHM parametrization at $z \sim 10$ and the systematic uncertainty introduced by summing the stellar masses within the two clumps (rather than including all the spaxels in Fig. 13c). The virial radius of the halo can be estimated using:

$$M_{\rm h} = \frac{4\pi}{3}\,\Delta_{\rm vir}\rho_{\rm m}(z)\,R_{\rm vir}^3. \quad (8)$$

In this equation, we assume that the density contrast is $\Delta_{\rm vir} = 200$, obtaining $R_{\rm vir} \approx 8.8 \pm 2.2$ kpc. Next, we estimate the concentration parameter $c_{200} = R_{\rm vir}/r_{\rm b} = 4.2 \pm 0.2$ from fig. 7 of L. Y. A. Yung et al. (2024). This implies $r_b = 2.1 \pm 0.5$ kpc. Under the spherical symmetry assumption, integrating the DM density profile would yield the following formula for the DM mass enclosed within a radius r:

$$M_{\rm DM}\,(<r) = M_{\rm vir}\,\frac{\ln\left(1+\dfrac{r}{r_{\rm b}}\right)-\dfrac{r/r_{\rm b}}{1+r/r_{\rm b}}}{\ln(1+c_{\rm vir})-\dfrac{c_{\rm vir}}{1+c_{\rm vir}}}. \quad (9)$$

Within the innermost $r = 200\,\text{pc}$ corresponding to the two clumps, we thus obtain $\log\,(M_{\rm DM}/{\rm M}_{\odot}) = 8.2 \pm 0.3$. These findings suggest that stars, gas, and DM have similar contributions to the total mass budget of the system. Therefore, it is currently difficult to estimate the spatial distribution of gas or DM in this system. Fig. 13(c) illustrates a clear double-peaked stellar-mass density distribution, with two spatially distinct mass concentrations corresponding to the southeastern and northwestern stellar components. For a disc-like galaxy to maintain long-term gravitational stability, however, the total mass (including stars, gas, and DM) profile should be centrally peaked (A. B. Romeo & K. M. Mogotsi 2018). Because a detailed analysis of the distributions of gas and DM within this system is currently impossible, the spatially resolved map of the total mass cannot be determined accurately. In conclusion, it is not possible to infer the dynamical nature of the system based entirely on the available M_* spatial distribution.

6 SUMMARY AND CONCLUSIONS

In this paper, we present a spatially resolved analysis of the ISM in MACS0647-JD1, the brightest galaxy currently known at $z > 10$ (owing to gravitational lensing), using medium-resolution NIRSpec/IFU *G*395*M* observations from the GA-NIFS GTO programme. We present a novel method for extrapolating the *JWST* spectra outside the nominal wavelength range of the *G*395*M* grating, enabling us to obtain the Hβ-wavelength collapsed flux map for a target at $z \sim 10.2$. By combining these spectroscopic data with archival *JWST* imaging, we infer SFHs across different regions of the system, enabling a detailed investigation of the physical processes governing its early assembly. This approach provides new insight into the complex interplay between star formation activity and chemical enrichment in one of the earliest known starburst systems. We summarize our conclusions as follows:

(i) The system consists of two bright components detected in NIRSpec/IFU and NIRCam imaging. The stellar continuum centroid coincides with the more massive component, which is spatially offset relative to the emission-line centroid by 150 pc (in the source plane). This is most likely a signpost of recent star formation activity in between the two components, potentially triggered by a pre-coalescence merger event.

(ii) Our target provides the highest redshift direct-metallicity measurement obtained with NIRSpec, and the second highest redshift measurement with any instrument, surpassed only by GN-z11 (A. J. Bunker et al. 2023; J. Álvarez-Márquez et al. 2025). We compute metallicities from spaxel spectra using two independent approaches: the direct method (based on the electron temperature) and a customized strong-line calibration. Both methods yield consistent results within the uncertainties. We find that the brighter southeastern clump is more metal-rich ($12 + \log({\rm O/H})_{\rm direct} = 7.89 \pm 0.11$), while the northwestern clump is less enriched ($12 + \log({\rm O/H})_{\rm direct} = 7.47 \pm 0.14$). Such a pronounced asymmetry would be difficult to explain if the two components were clumps within a single rotating disc. Although we attempted to reconstruct the velocity field (see Appendix C), the current data do not provide conclusive evidence for ordered rotation.

(iii) The strong-line metallicities are less reliable in the southwestern part, where the unusual morphology of the [O II] $\lambda\lambda$3726, 3729 emission (as compared to high-ionization or hydrogen recombination lines), together with tentative AGN-like signatures on one of the G. Mazzolari et al. (2024) diagnostic diagrams, may imply the presence of DIG or a complex stratification structure. We have additionally shown that shocks are strongly disfavoured, although not completely ruled out by our observed emission-line ratios.

(iv) We analyse the ISM conditions on spatially resolved scales by focusing on various diagnostic ratios. Analysing the spectra of individual spaxels, we find a meaningful anticorrelation between the gas velocity dispersion (FWHM; a tracer of turbulence) and [O III] λ4363/Hγ line ratio (a proxy for the excitation state of the ISM), but statistically weaker trends between FWHM and gas-phase metallicity or electron temperature, both of which are likely influenced by a secondary dependence on the ionization parameter.

(v) Combining our spectroscopic and stellar populations analyses, we demonstrate that, remarkably, the northeastern region has a small stellar mass and predominantly contains metal-poor gas, while its star formation burstiness is significantly elevated compared to the surroundings. This suggests that a very recent star formation event has been initiated in that region, which could be either associated with a fresh gas inflow or a redistribution of the metal-poor gas already present in the northwestern component, as a result of gravitational interaction. These two scenarios could explain the metallicity difference between the southeastern and northwestern components, which are massive gas clumps, with only low to moderate burstiness.

ACKNOWLEDGEMENTS

We are grateful to the referee for insightful and constructive feedback that substantially improved the quality of this manuscript. We thank Doctor Xihan Ji, Professor Alessandro Romeo, and Doctor Guochao Sun for insightful comments that led to a better interpretation of our results in the context of recent developments in the theoretical models of bursty star formation at high redshift. Robert-Gabriel Pascalau acknowledges funding support from an Science and Technology Facilities Council (STFC) PhD studentship. Robert-Gabriel Pascalau, Francesco D'Eugenio, Roberto Maiolino, Gareth C. Jones, Jan Scholtz, and Lucy R. Ivey acknowledge support by the Science and Technology Facilities Council (STFC), by the European Research Council (ERC) through Advanced Grant 695671 'QUENCH', and by the United Kingdom Research and Innovation (UKRI) Frontier Research grant RISEandFALL. Roberto Maiolino also acknowledges funding from a research professorship from the Royal Society. Qiao Duan acknowledges a PhD studentship from Trinity College, Cambridge. Yuki Isobe is supported by Japan Society for the Promotion of Science (JSPS) KAKENHI grant numbers 24KJ0202 and 24KJ1160. Hannah Übler acknowledges funding by the European Union (European Research Council APEX 101164796). Views and opinions expressed are however those of the authors only and do not necessarily reflect those of the European Union or the European Research Council Executive Agency. Neither the European Union nor the granting authority can be held responsible for them. Sandra Zamora, Stefano Carniani, and Giacomo Venturi acknowledge support from the European Union's European Research Council Starting grant number 101040227 – WINGS. Isabella Lamperti acknowledges support from PRIN-MUR project 'PROMETEUS' financed by the European Union – Next Generation European Union, Mission 4 Component 1 CUP B53D23004750006. Andrew J. Bunker and Gareth C. Jones acknowledge funding from the 'FirstGalaxies' Advanced Grant from the European Research Council (ERC) under the European Union's Horizon 2020 research and innovation program (grant agreement number 789056). Bruno Rodriguez del Pino, Santiago Arribas, and Michele Perna acknowledge grant PID2021-127718NB-I00 funded by the Spanish Ministry of Science and Innovation/State Agency of Research (MICIN/AEI/ 10.13039/501100011033); Michele Perna also acknowledges the grants RYC2023-044853-I and PID2024-159902NA-I00, funded by MICIU/AEI/10.13039/501100011033 and European Social Fund Plus (FSE+). Bruno Rodriguez del Pino also acknowledges support by the grant PID2024-158856NA-I00. MC acknowledges support from European Southern Observatory (ESO) via the ESO Fellowship Europe. Elena Bertola and Giovanni Cresci acknowledge the Istituto Nazionale di Astrofisica (INAF) GO grant 'A JWST/MIRI MIRACLE: Mid-IR Activity of Circumnuclear Line Emission' and the 'Ricerca Fondamentale 2024' Istituto Nazionale di Astrophisica program (mini-grant 1.05.24.07.01). Tiger Hsiao was supported by JSPS KAKENHI 25K00020. Sandro Tacchella acknowledges support from the Royal Society Research Grant G125142. JW acknowledges support from the Cosmic Dawn Center through the DAWN Fellowship; the Cosmic Dawn Center (DAWN) is funded by the Danish National Research Foundation under grant no. 140.

DATA AVAILABILITY

This work is based on observations with the NASA/ESA/CSA *James Webb Space Telescope*. The data were obtained as part of the *JWST* programme ID 4528 (Cycle 3, PI: K. Isaak). These data are available from Mikulski Archive for Space Telescopes at the Space Telescope Science Institute, which is operated by the Association of Universities for Research in Astronomy, Inc., under NASA contract NAS 5-03127 for *JWST*. The reduced datacube is available upon reasonable request. The photometry data are available from the public DAWN JWST Archive (DJA) data.[5]

REFERENCES

Abazajian K. N. et al., 2009, ApJS, 182, 543
Abdurro'uf et al., 2024, ApJ, 973, 47
Agertz O. et al., 2020, MNRAS, 491, 1656
Alarie A., Morisset C., 2019, Rev. Mex. Astron. Astrofis., 55, 377
Allen M. G., Groves B. A., Dopita M. A., Sutherland R. S., Kewley L. J., 2008, ApJS, 178, 20
Álvarez-Márquez J. et al., 2025, A&A, 695, A250
Arellano-Córdova K. Z. et al., 2022, ApJ, 940, L23
Arribas S. et al., 2024, A&A, 688, A146
Astropy Collaboration, 2022, ApJ, 935, 167
Bacon R. et al., 1995, A&AS, 113, 347
Baker W. M. et al., 2023, MNRAS, 519, 1149
Baker W. M. et al., 2025, A&A, 697, A90

[5]Available at https://s3.amazonaws.com/grizli-v2/JwstMosaics/v7/index.html

Beck R., 2015, A&AR, 24, 4
Beck T., 2025, Technical Report Technical Report JWST-STScI-009029, Evidence for Problems in the JWST NIRSpec IFU Calibration Distortion Model. STScI
Behroozi P., Wechsler R. H., Hearin A. P., Conroy C., 2019, MNRAS, 488, 3143
Bezanson R. et al., 2018, ApJ, 868, L36
Böker T. et al., 2022, A&A, 661, A82
Bouché N. et al., 2007, ApJ, 671, 303
Bourne M. A., Yang H.-Y. K., 2023, Galaxies, 11, 73
Boyett K. et al., 2024, MNRAS, 535, 1796
Bradley L. et al., 2024, astropy/photutils: 2.0.2.
Brammer G., 2023, grizli
Bunker A. J. et al., 2023, A&A, 677, A88
Bunker A. J. et al., 2024, A&A, 690, A288
Byler N., Dalcanton J. J., Conroy C., Johnson B. D., 2017, ApJ, 840, 44
Calabrò A. et al., 2024, ApJ, 975, 245
Calzetti D., Armus L., Bohlin R. C., Kinney A. L., Koornneef J., Storchi-Bergmann T., 2000, ApJ, 533, 682
Cameron A. J. et al., 2023, A&A, 677, A115
Cappellari M., 2017, MNRAS, 466, 798
Cappellari M., 2023, MNRAS, 526, 3273
Cappellari M. et al., 2006, MNRAS, 366, 1126
Carniani S. et al., 2024, Nature, 633, 318
Castellano M. et al., 2024, ApJ, 972, 143
Cataldi E. et al., 2025, A&A, 703, A208
Chabrier G., 2003, PASP, 115, 763
Chan B. M. Y., Broadhurst T., Lim J., Diego J. M., Zitrin A., Coe D., Ford H. C., 2017, ApJ, 835, 44
Charlot S., Fall S. M., 2000, ApJ, 539, 718
Chen Y. et al., 2023, Nat. Astron., 7, 771
Choi J., Dotter A., Conroy C., Cantiello M., Paxton B., Johnson B. D., 2016, ApJ, 823, 102
Choustikov N. et al., 2026, Open J. Astrophys., 9, 58199
Christensen L. et al., 2012, MNRAS, 427, 1953
Claeyssens A., Adamo A., Richard J., Mahler G., Messa M., Dessauges-Zavadsky M., 2023, MNRAS, 520, 2180
Clarendon A., Strom A., von Raesfeld C., 2025, Res. Notes Am. Astron. Soc., 9, 206
Coe D. et al., 2013, ApJ, 762, 32
Conroy C., Gunn J. E., 2010, ApJ, 712, 833
Conroy C. et al., 2009, ApJ, 699, 486
Costantin L. et al., 2023, ApJ, 946, 71
Covelo-Paz A. et al., 2026, A&A, 705, A155
Curti M. et al., 2023, MNRAS, 518, 425
Curti M. et al., 2024, A&A, 684, A75
Curti M. et al., 2025, A&A, 697, A89
Curtis-Lake E. et al., 2023, Nat. Astron., 7, 622
D'Eugenio F. et al., 2024a, Nat. Astron., 8, 1443
D'Eugenio F. et al., 2024b, A&A, 689, A152
D'Eugenio F. et al., 2026a, MNRAS, 547, 401
D'Eugenio F. et al., 2025b, ApJS, 277, 4
D'Eugenio F. et al., 2025c, MNRAS, 536, 51
D'Eugenio F. et al., 2025d, MNRAS, 542, 960
Danhaive A. L. et al., 2025, MNRAS, 543, 3249
Danhaive A. L. et al., 2026a, MNRAS, 546
Danhaive A. L. et al., 2026b, MNRAS, 547, stag437
Davé R., Finlator K., Oppenheimer B. D., 2011, MNRAS, 416, 1354
de Graaff A. et al., 2024a, A&A, 684, A87
de Graaff A., Pillepich A., Rix H.-W., 2024b, ApJ, 967, L40
De Lucia G., Xie L., Fontanot F., Hirschmann M., 2020, MNRAS, 498, 3215
De Rossi M. E., Bower R. G., Font A. S., Schaye J., Theuns T., 2017, MNRAS, 472, 3354
Dekel A. et al., 2009, Nature, 457, 451
Díaz A. I., Castellanos M., Terlevich E., Luisa García-Vargas M., 2000, MNRAS, 318, 462
Dome T., Tacchella S., Fialkov A., Ceverino D., Dekel A., Ginzburg O., Lapiner S., Looser T. J., 2024, MNRAS, 527, 2139

Donnan C. T. et al., 2025, ApJ, 993, 224
Dorner B. et al., 2016, A&A, 592, A113
Dors O. L., Maiolino R., Cardaci M. V., Hägele G. F., Krabbe A. C., Pérez-Montero E., Armah M., 2020, MNRAS, 496, 3209
Dressler A. et al., 2024, ApJ, 964, 150
Duan Q., Conselice C. J., Li Q., Harvey T., Austin D., Ormerod K., Trussler J., Adams N., 2024, MNRAS, 529, 4728
Duan Q. et al., 2025, MNRAS, 540, 774
Duan Q. et al., 2026a, preprint (arXiv:2605.21599)
Duan Q. et al., 2026b, MNRAS, 546, stag008
Ebeling H., Barrett E., Donovan D., Ma C. J., Edge A. C., van Speybroeck L., 2007, ApJ, 661, L33
Endsley R., Chisholm J., Stark D. P., Topping M. W., Whitler L., 2025, ApJ, 987, 189
Fabian A. C., 2012, ARA&A, 50, 455
Falcón-Barroso J. et al., 2011, A&A, 532, A95
Faucher-Giguère C.-A., 2018, MNRAS, 473, 3717
Ferland G. J. et al., 2013, Rev. Mex. Astron. Astrofis., 49, 137
Ferland G. J. et al., 2017, Rev. Mex. Astron. Astrofis., 53, 385
Ferrara A., Pallottini A., Sommovigo L., 2025, A&A, 694, A286
Ford H. C. et al., 2003, in Future EUV/UV and Visible Space Astrophysics Missions and Instrumentation. p. 81
Foreman-Mackey D., Hogg D. W., Lang D., Goodman J., 2013, PASP, 125, 306
Förster Schreiber N. M., Wuyts S., 2020, ARA&A, 58, 661
Fujimoto S. et al., 2023, ApJ, 949, L25
Fujimoto S. et al., 2024, ApJ, 977, 250
Fujimoto S. et al., 2025a, preprint (arXiv:2510.16116)
Fujimoto S. et al., 2025b, Nat. Astron., 9, 1553
Garcia A. M. et al., 2024, MNRAS, 531, 1398
Garcia A. M. et al., 2026, ApJ, 1001, 188
Gardner J. P. et al., 2023, PASP, 135, 068001
Garg P., Narayanan D., Sanders R. L., Davé R., Popping G., Shapley A. E., Stark D. P., Trump J. R., 2024, ApJ, 972, 113
Geris S. et al., 2026, MNRAS, 545, staf1979
Gibson B. K., Pilkington K., Brook C. B., Stinson G. S., Bailin J., 2013, A&A, 554, A47
Greene J. E. et al., 2024, ApJ, 964, 39
Groves B., Brinchmann J., Walcher C. J., 2012, MNRAS, 419, 1402
Gutkin J., Charlot S., Bruzual G., 2016, MNRAS, 462, 1757
Hainline K. N. et al., 2024, ApJ, 964, 71
Harikane Y., Nakajima K., Ouchi M., Umeda H., Isobe Y., Ono Y., Xu Y., Zhang Y., 2024, ApJ, 960, 56
Harikane Y. et al., 2025, ApJ, 993, 204
Harvey T. et al., 2025, ApJ, 978, 89
Hayes M. J., Saldana-Lopez A., Citro A., James B. L., Mingozzi M., Scarlata C., Martinez Z., Berg D. A., 2025, ApJ, 982, 14
Heintz K. E. et al., 2023, Nat. Astron., 7, 1517
Heintz K. E. et al., 2024, Science, 384, 890
Heintz K. E. et al., 2025, A&A, 693, A60
Herrera-Camus R. et al., 2025, A&A, 699, A80
Hopkins P. F., Kereš D., Oñorbe J., Faucher-Giguère C.-A., Quataert E., Murray N., Bullock J. S., 2014, MNRAS, 445, 581
Hopkins P. F. et al., 2023, MNRAS, 525, 2241
Hsiao T. Y.-Y. et al., 2023, ApJ, 949, L34
Hsiao T. Y.-Y. et al., 2024a, ApJ, 973, 8
Hsiao T. Y.-Y. et al., 2024b, ApJ, 973, 81
Hsiao T. Y.-Y. et al., 2025, ApJ, 993, 70
Huertas-Company M. et al., 2024, A&A, 685, A48
Hunter D. A., Gallagher III J. S., 1990, ApJ, 362, 480
Hutchison T. A. et al., 2025, preprint (arXiv:2512.02000)
Inoue A. K., Shimizu I., Iwata I., Tanaka M., 2014, MNRAS, 442, 1805
Isobe Y. et al., 2023a, ApJ, 951, 102
Isobe Y., Ouchi M., Nakajima K., Harikane Y., Ono Y., Xu Y., Zhang Y., Umeda H., 2023b, ApJ, 956, 139
Ivey L. R. et al., 2026a, MNRAS
Ivey L. R. et al., 2026b, MNRAS, 546, stag094
Iyer K. G. et al., 2020, MNRAS, 498, 430
Izotov Y. I., Stasińska G., Meynet G., Guseva N. G., Thuan T. X., 2006, A&A, 448, 955
Jakobsen P. et al., 2022, A&A, 661, A80
Ji X., Belokurov V., Maiolino R., Monty S., Isobe Y., Kravtsov A., McClymont W., Übler H., 2026, MNRAS, 545, staf2110
Johnson B. D., Leja J., Conroy C., Speagle J. S., 2021, ApJS, 254, 22
Jones T., Sanders R., Roberts-Borsani G., Ellis R. S., Laporte N., Treu T., Harikane Y., 2020, ApJ, 903, 150
Jones G. C. et al., 2024, A&A, 682, A122
Jones G. C. et al., 2025a, preprint (arXiv:2512.05213)
Jones G. C. et al., 2025b, MNRAS, 540, 3311
Jones G. C. et al., 2026a, MNRAS, 546, stag115
Jones G. C. et al., 2026b, MNRAS, 547, stag336
Juodžbalis I. et al., 2026, MNRAS, 546, stag086
Kashikawa N. et al., 2002, PASJ, 54, 819
Kashino D., Lilly S. J., Matthee J., Eilers A.-C., Mackenzie R., Bordoloi R., Simcoe R. A., 2023, ApJ, 950, 66
Kennicutt R. C., Jr, 1998, ARA&A, 36, 189
Kennicutt R. C., Evans N. J., 2012, ARA&A, 50, 531
Kereš D., Katz N., Weinberg D. H., Davé R., 2005, MNRAS, 363, 2
Kewley L. J., Dopita M. A., 2002, ApJS, 142, 35
Kewley L. J., Ellison S. L., 2008, ApJ, 681, 1183
Kimble R. A., MacKenty J. W., O'Connell R. W., Townsend J. A., 2008, in Space Telescopes and Instrumentation 2008: Optical, Infrared, and Millimeter. p. 70101E
Lamperti I. et al., 2024, A&A, 691, A153
Langeroodi D., Hjorth J., 2023, preprint (arXiv:2307.06336)
Langeroodi D., Hjorth J., 2024, preprint (arXiv:2404.13045)
Langeroodi D. et al., 2023, ApJ, 957, 39
Laor A., 1998, ApJ, 496, L71
Laseter I. H. et al., 2024, A&A, 681, A70
Le Fèvre O. et al., 2020, A&A, 643, A1
Leja J., Carnall A. C., Johnson B. D., Conroy C., Speagle J. S., 2019, ApJ, 876, 3
Lequeux J., Peimbert M., Rayo J. F., Serrano A., Torres-Peimbert S., 1979, A&A, 80, 155
Levesque E. M., Richardson M. L. A., 2014, ApJ, 780, 100
Li H. et al., 2018, MNRAS, 476, 1765
Li J. et al., 2025, ApJ, 981, 19
Lilly S. J., Carollo C. M., Pipino A., Renzini A., Peng Y., 2013, ApJ, 772, 119
Looser T. J. et al., 2024, Nature, 629, 53
Looser T. J. et al., 2025, A&A, 697, A88
Luridiana V., Morisset C., Shaw R. A., 2015, A&A, 573, A42
Lützgendorf N. et al., 2022, in Coyle L. E., Matsuura S., Perrin M. D., eds, Proc. SPIE Conf. Ser. Vol. 12180, Space Telescopes and Instrumentation 2022: Optical, Infrared, and Millimeter Wave. p. 121800Y, preprint (arXiv:2208.05355)
Ma X. et al., 2018, MNRAS, 478, 1694
Maiolino R., Mannucci F., 2019, A&AR, 27, 3
Maiolino R. et al., 2008, A&A, 488, 463
Marconcini C. et al., 2024, MNRAS, 533, 2488
Marconcini C. et al., 2025, A&A, 699, A154
Marconi A. et al., 2024, A&A, 689, A78
Marshall M. A. et al., 2023, A&A, 678, A191
Marshall M. A. et al., 2025a, A&A, 702, A50
Marshall M. A. et al., 2025b, A&A, 702, A174
Martinez Z. et al., 2025, ApJ, 995, 204
Mascia S. et al., 2023, A&A, 672, A155
Mason C. A., Trenti M., Treu T., 2023, MNRAS, 521, 497
Matharu J. et al., 2024, A&A, 690, A64
Mazzolari G. et al., 2024, A&A, 691, A345
Mazzolari G. et al., 2025, A&A, 700, A12
McClymont W. et al., 2024, MNRAS, 532, 2016
McClymont W. et al., 2025, MNRAS, 544, 513
McClymont W. et al., 2026, MNRAS, 545, staf2092
Miller T. B. et al., 2025, ApJ, 988, 196

Moreschini B. et al., 2026, preprint (arXiv:2601.08939)
Morishita T. et al., 2024, ApJ, 971, 43
Mott A., Spitoni E., Matteucci F., 2013, MNRAS, 435, 2918
Mowla L. et al., 2022, ApJ, 937, L35
Mowla L. et al., 2024, Nature, 636, 332
Nagao T., Maiolino R., Marconi A., 2006, A&A, 459, 85
Naidu R. P. et al., 2026, Open J. Astrophys., 9, 56033
Nakajima K. et al., 2022, ApJS, 262, 3
Nakajima K., Ouchi M., Isobe Y., Harikane Y., Zhang Y., Ono Y., Umeda H., Oguri M., 2023, ApJS, 269, 33
Nakajima K. et al., 2026, Nature, 653, 363
Nakazato Y., Yoshida N., Ceverino D., 2023, ApJ, 953, 140
Napolitano L. et al., 2025, A&A, 693, A50
Navarro J. F., Frenk C. S., White S. D. M., 1996, ApJ, 462, 563
Noll S., Burgarella D., Giovannoli E., Buat V., Marcillac D., Muñoz-Mateos J. C., 2009, A&A, 507, 1793
Oesch P. A. et al., 2023, MNRAS, 525, 2864
Oke J. B., Gunn J. E., 1983, ApJ, 266, 713
Osterbrock D. E., 1989, Astrophysics of Gaseous Nebulae and Active Galactic Nuclei
Ozaki S. et al., 2020, PASJ, 72, 97
Papovich C. et al., 2022, ApJ, 937, 22
Parlanti E. et al., 2025a, preprint (arXiv:2512.14844)
Parlanti E. et al., 2025b, A&A, 695, A6
Pascalau R. G. et al., 2026, MNRAS, 547, stag210
Peimbert M., 1967, ApJ, 150, 825
Pérez-González P. G. et al., 2025, Nat. Astron., 9, 1240
Pérez-Montero E., Hägele G. F., Contini T., Díaz Á. I., 2007, MNRAS, 381, 125
Perna M. et al., 2023, A&A, 679, A89
Perna M. et al., 2025, A&A, 696, A59
Péroux C., Howk J. C., 2020, ARA&A, 58, 363
Planck Collaboration VI, 2020, A&A, 641, A6
Pollock C. L. et al., 2026, A&A, 708, A203
Price S. H. et al., 2025, ApJ, 982, 51
Puskás D. et al., 2025a, preprint (arXiv:2510.14743)
Puskás D. et al., 2025b, MNRAS, 540, 2146
Rauscher B. J. et al., 2017, PASP, 129, 105003
Reddy N. A. et al., 2022, ApJ, 926, 31
Reddy N. A., Topping M. W., Sanders R. L., Shapley A. E., Brammer G., 2023, ApJ, 952, 167
Rigby J. et al., 2023, PASP, 135, 048001
Roberts-Borsani G. et al., 2023, Nature, 618, 480
Robertson B. E. et al., 2023, Nat. Astron., 7, 611
Rodríguez Del Pino B. et al., 2024, A&A, 684, A187
Rodríguez Del Pino B. et al., 2026, A&A, 711, A66
Romeo A. B., Mogotsi K. M., 2017, MNRAS, 469, 286
Romeo A. B., Mogotsi K. M., 2018, MNRAS, 480, L23
Roper W. J., Lovell C. C., Vijayan A. P., Marshall M. A., Irodotou D., Kuusisto J. K., Thomas P. A., Wilkins S. M., 2022, MNRAS, 514, 1921
Sánchez S. F. et al., 2017, MNRAS, 469, 2121
Sanders R. L. et al., 2016, ApJ, 816, 23
Sanders R. L. et al., 2023a, ApJ, 943, 75
Sanders R. L., Shapley A. E., Topping M. W., Reddy N. A., Brammer G. B., 2023b, ApJ, 955, 54
Sanders R. L., Shapley A. E., Topping M. W., Reddy N. A., Brammer G. B., 2024, ApJ, 962, 24
Sanders R. L. et al., 2026, ApJ, 1003, 228
Scarlata C., Hayes M., Panagia N., Mehta V., Haardt F., Bagley M., 2024, preprint (arXiv:2404.09015)
Schaerer D., Marques-Chaves R., Xiao M., Korber D., 2024, A&A, 687, L11
Schaye J. et al., 2010, MNRAS, 402, 1536
Scholte D. et al., 2025, MNRAS, 540, 1800
Scholtz J. et al., 2025a, MNRAS, 539, 2463
Scholtz J. et al., 2025b, A&A, 697, A175
Scholtz J. et al., 2026, MNRAS, 545, staf2107
Schwarz G., 1978, Ann. Stat., 6, 461
Shajib A. J., Treu T., Melo A., Roberts-Borsani G., Knabel S., Cappellari M., Frieman J. A., 2025, A&A, 702, L12
Shapley A. E. et al., 2017, ApJ, 846, L30
Shapley A. E., Sanders R. L., Reddy N. A., Topping M. W., Brammer G. B., 2023, ApJ, 954, 157
Shapley A. E. et al., 2025, ApJ, 981, 167
Shen X. et al., 2024, MNRAS, 534, 1433
Shibuya T., Ouchi M., Harikane Y., 2015, ApJS, 219, 15
Shivaei I. et al., 2020, ApJ, 899, 117
Sánchez-Blázquez P. et al., 2006, MNRAS, 371, 703
Somerville R. S., Davé R., 2015, ARA&A, 53, 51
Sparre M., Hayward C. C., Feldmann R., Faucher-Giguère C.-A., Muratov A. L., Kereš D., Hopkins P. F., 2017, MNRAS, 466, 88
Stasińska G., Tenorio-Tagle G., Rodríguez M., Henney W. J., 2007, A&A, 471, 193
Stephenson H. M. O. et al., 2025, MNRAS, 544, 1412
Stiavelli M. et al., 2025, ApJ, 981, 136
Strait V. et al., 2023, ApJ, 949, L23
Sun G., Faucher-Giguère C.-A., Hayward C. C., Shen X., Wetzel A., Cochrane R. K., 2023, ApJ, 955, L35
Sun X. et al., 2025, ApJ, 986, 179
Sun G., Faucher-Giguère C.-A., Stern J., 2026, ApJ, 996, 139
Sutherland R. S., Dopita M. A., 2017, ApJS, 229, 34
Tacchella S., Forbes J. C., Caplar N., 2020, MNRAS, 497, 698
Tacchella S. et al., 2022a, ApJ, 926, 134
Tacchella S. et al., 2022b, ApJ, 927, 170
Tacchella S. et al., 2023, MNRAS, 522, 6236
Tang M. et al., 2023, MNRAS, 526, 1657
Topping M. W. et al., 2024, MNRAS, 529, 3301
Topping M. W. et al., 2025a, MNRAS, 541, 1707
Topping M. W. et al., 2025b, ApJ, 980, 225
Torralba A. et al., 2026, A&A, 707, A75
Tremonti C. A. et al., 2004, ApJ, 613, 898
Tripodi R. et al., 2024, A&A, 692, A184
Troncoso P. et al., 2014, A&A, 563, A58
Trump J. R. et al., 2023, ApJ, 945, 35
Übler H. et al., 2023, A&A, 677, A145
Übler H. et al., 2024, MNRAS, 533, 4287
Übler H. et al., 2025, preprint (arXiv:2509.21575)
Valentino F. et al., 2023, ApJ, 947, 20
Valentino F. et al., 2025, A&A, 699, A358
Vallee J. P., 2022, Int. J. Astron. Astrophys., 12, 281
Vanzella E. et al., 2023, A&A, 678, A173
van der Wel A. et al., 2022, ApJ, 936, 9
van Dokkum P. G., 2001, PASP, 113, 1420
Venturi G. et al., 2024, A&A, 691, A19
Venturi G. et al., 2025, preprint (arXiv:2512.09996)
Wang W., Liu X.-W., Zhang Y., Barlow M. J., 2004, A&A, 427, 873
Wang B. et al., 2023a, ApJ, 944, L58
Wang B. et al., 2023b, ApJ, 957, L34
Weinberger R. et al., 2017, MNRAS, 465, 3291
Witstok J., Smit R., Maiolino R., Curti M., Laporte N., Massey R., Richard J., Swinbank M., 2021, MNRAS, 508, 1686
Witten C. et al., 2025, MNRAS, 537, 112
Wolfe A. M., Jorgenson R. A., Robishaw T., Heiles C., Prochaska J. X., 2008, Nature, 455, 638
Wyithe J. S. B., Turner E. L., Spergel D. N., 2001, ApJ, 555, 504
Yajima H., Abe M., Fukushima H., Ono Y., Harikane Y., Ouchi M., Hashimoto T., Khochfar S., 2023, MNRAS, 525, 4832
Yang S., Lidz A., 2020, MNRAS, 499, 3417
Yang S., Lidz A., Popping G., 2021, MNRAS, 504, 723
Yang L. et al., 2025, ApJS, 281, 68
Yung L. Y. A., Somerville R. S., Nguyen T., Behroozi P., Modi C., Gardner J. P., 2024, MNRAS, 530, 4868
Zamora S. et al., 2025a, preprint (arXiv:2512.09022)
Zamora S. et al., 2025b, A&A, 702, A102
Zavala J. A. et al., 2025, Nat. Astron., 9, 155
Zhang K. et al., 2017, MNRAS, 466, 3217

APPENDIX A: EMISSION-LINE MAPS

This appendix presents images of integrated fluxes maps for a number of key rest-frame optical emission lines, together with the corresponding wavelength slices of the datacube. All these maps show that high-ionization and Balmer recombination emission are mostly constrained to the very central part of MACS0647-JD1. The central region between the two stellar clumps (Fig. 2b) hosts the most intense recent star-formation activity, and, consequently, the most intense line emission. In contrast, the outskirts of the system show more pronounced emission from the low-ionization gas traced via [O II] λ3726, 3729 emission.

APPENDIX B: FURTHER SPATIALLY RESOLVED EMISSION-LINES DIAGNOSTICS

In Fig. B1, we report spaxel-by-spaxel maps of O_{33} and O_{32} diagnostic ratios (as defined in the main text of Section 4.1 and following the criteria and demarcation lines identified by G. Mazzolari et al. 2024). In the case of both diagnostics, all spaxels reside below the 'AGN-only' regime, revealing that AGN is likely not the main excitation source of the ISM in neither region of this galaxy.

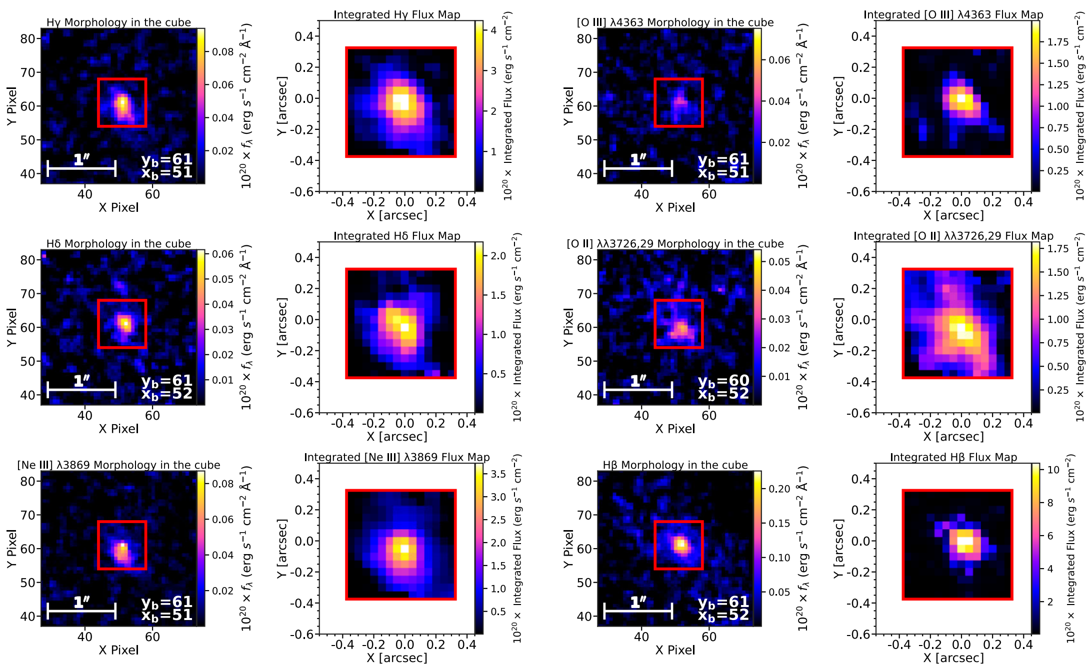

Figure A1. This figure displays a comparison between the images obtained by collapsing the PSF-matched datacube (see Section 3.1 for details of the PSF-matching method) along the wavelength slices corresponding to our key emission lines and the images resulting from mapping out the integrated fluxes of these emission lines which were determined by our MCMC spectral-fitting analysis. We remark on small shifts between the centroids of different emission lines (identified by the coordinates y_b and x_b of the brightest spaxel for each emission-line map) but this is not worrying given that these differences are on the order of ~ 1 spaxel. This centroid drift as a function of wavelength is likely to be caused by a combination of filter transmission effects and imperfect NIRSpec/IFU calibrations.

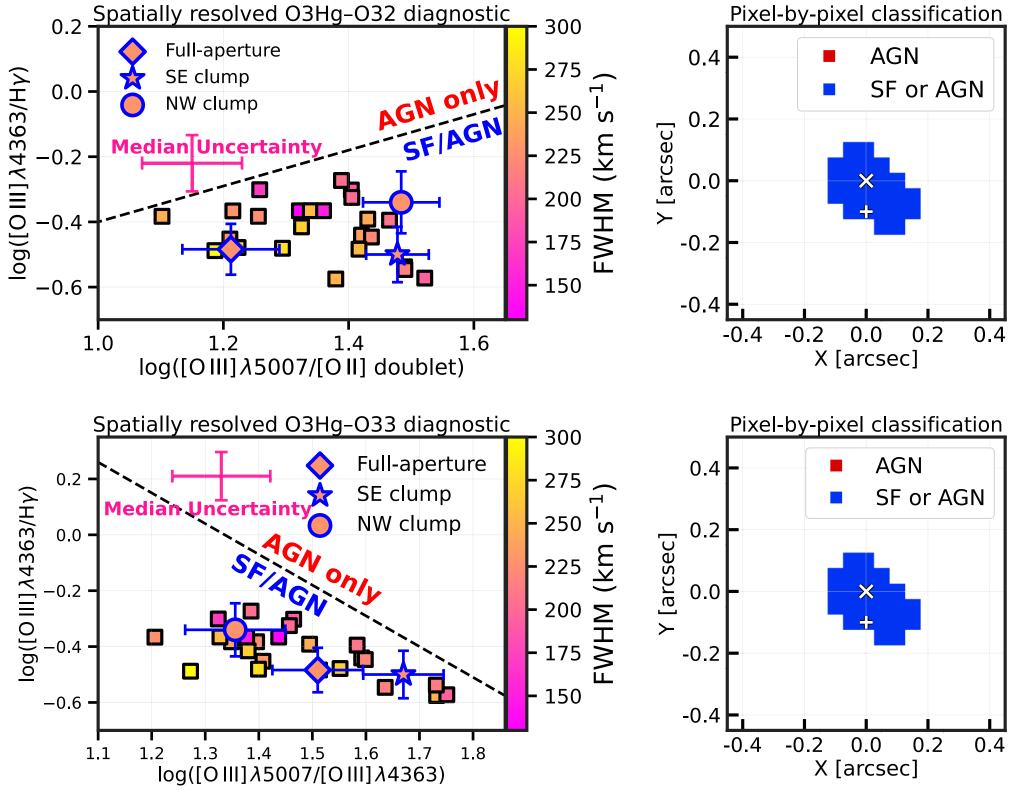

Figure B1. This diagram is equivalent (in terms of labelling and the meaning of various symbols) to Fig. 6, which presents the O_3Hg versus Ne_3O_2 diagnostic diagram on a spatially resolved spaxel-by-spaxel scale. However, alternative AGN versus SFG diagnostics (G. Mazzolari et al. 2024) are illustrated: O_3Hg–O_{32} **(**top panels**)** and O_3Hg–O_{33} (bottom panels). We can remark that, in contrast to the results based on the diagnostic $O_3Hg - Ne_3O_2$ (from Fig. 6, showing the presence of a south-southwest AGN-dominated region), if we use either $O_3Hg - O_{32}$ or $O_3Hg - O_{33}$ diagnostics, we would observe that all regions of the MACS0647-JD1 system are either dominated by star-formation-driven photoionization or the contribution of SF and AGN are similar.

APPENDIX C: ON THE VELOCITY FIELD OF MACS0647-JD1

In Fig. C2(a), we present the spatially resolved maps of Δv (velocity shift of a particular spaxel with respect to galaxy's systemic velocity). We obtain Δv from the MCMC-fitted redshift corresponding to each spaxel spectrum:

$$(1 + z_{\rm pix}) = (1 + z_{\rm pix,med}) \times (1 + \Delta v/c)\ . \quad \text{(C1)}$$

Here, the median redshift of the spaxels is $z_{\rm pix,med} = 10.1672$. The fact that the direction of the rotational gradient approximately coincides with the direction of IFU slicers, together with the relatively small amplitude of 160 km s^{-1} ($\sim$ 1.45 spectral pixels, peak to peak) makes it uncertain whether the observed rotation is a real feature. This issue has been identified and documented, but no official solution has been proposed to date. Similar artificial rotation patterns have been reported in ground-based IFU observations obtained with the *Subaru*/FOCAS instrument (N. Kashikawa et al. 2002; S. Ozaki et al. 2020) and, more recently, in high spectral resolution IFU studies of high-redshift galaxies (L. R. Ivey et al. 2026a). In particular, Y. Isobe et al. (2023a) demonstrated that a differential effective slit width across the IFU slices can introduce spurious velocity gradients aligned with the instrumental geometry, thereby mimicking ordered rotation in emission-line velocity fields.

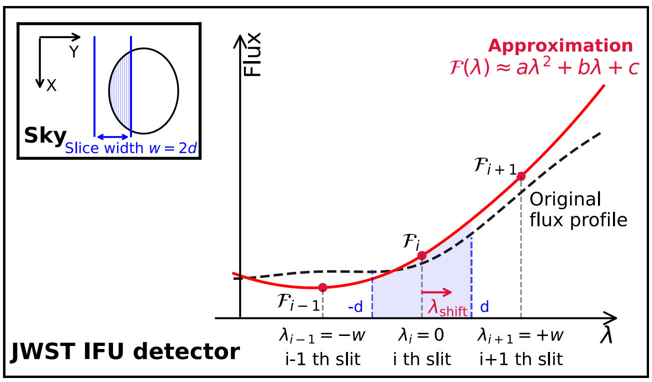

Figure C1. In this figure, we present a simplified explanation of the slit width effect. The main panel shows the flux profile projected onto the *JWST* NIRSpec/IFU detector (black dashed curve) and the measured fluxes $\mathcal{F}_{i-1}$, $\mathcal{F}_i$, and $\mathcal{F}_{i+1}$ on three adjacent slices. In this approach, the original flux profile is approximated with a quadratic function (the red solid curve) within a wavelength range $-w < \lambda < w$. The inset panel schematically shows an hypothetic circular object on the sky. The X (Y) direction denotes the direction of the slice length (width). The blue vertical lines in the inset panel show the position of the edges of the central slice. The light coming into the slice (blue hatched) is projected onto the detector, and the Y-direction in the sky is parallel to the dispersion (or wavelength) direction on the detector.

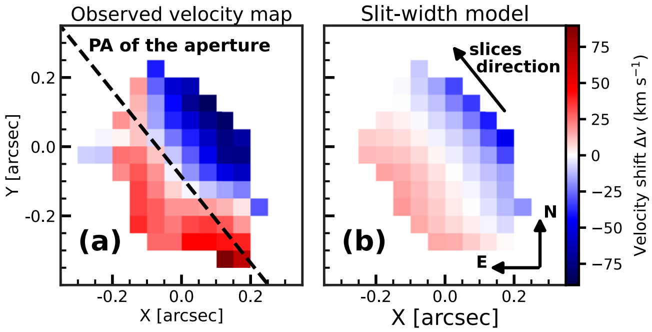

Figure C2. This figure shows the spatially resolved Δv (the velocity field) map derived from single-Gaussian component spaxel-by-spaxel spectral fits (a). We only show the spaxels with a solid detection of Hγ (S/N > 5). We also indicate the position angle of the aperture of these observations, PA = 38.83°, i.e. the direction of the NIRSpec/IFU slices. The velocity gradient of the observed rotational pattern is perpendicular to the direction of the slices. In (b), we show a mock velocity pattern resulting from the IFU slices geometrical model described in the text.

While the geometrical model implemented within the current pipeline typically succeeds in providing an accurate wavelength calibration (B. Dorner et al. 2016; N. Lützgendorf et al. 2022), a recent report by T. Beck (2025) argues that some imperfections in the current IFU spectral distortion model remain. Artificial kinematics shifts are observed for multiple grating/filter combinations and regardless of the cube weighting algorithms ('drizzle', 'EMSM', or 'MSM'). In the particular case of *G395M* grating that we used in our observations, T. Beck (2025) reports a peak-to-peak amplitude of the artificial kinematic shift of ~ 1.6 spectral pixels in the case of a planetary nebula with substantially lower intrinsic kinematics. This is similar to the amplitude of the velocity gradient in Fig. C2(a). However, it should be noted that the rotational pattern observed in our case is both more spatially extended (and larger than the PSF size), but also significantly less noisy (as there are less large kinematic variations in adjacent spaxels) than the pattern reported by T. Beck (2025).

In Fig. C2(b), we show that a simple geometrical model of the IFU slicer configuration (that is described and explained schematically in Fig. C1) can reproduce an artificial velocity pattern similar in amplitude and orientation to that observed in our data. The underlying effect arises from spatial variations in the emission-line surface brightness across the finite width of an IFU slice (R. Bacon et al. 1995). If we have a slice of projected width w on the IFU detector and with a flux profile $\mathcal{F}(\lambda)$ along the dispersion (wavelength) direction coordinate λ (perpendicular to the slit width direction), the effective centroid of the detected emission line can be shifted relative to the true wavelength. The method to quantify the magnitude of this wavelength shift is thoroughly described in Y. Isobe et al. (2023a), but here we give an outline of the numerical calculations. We can estimate the wavelength shift caused by the slit-width effect from a barycentre of the flux following a $\mathcal{F}(\lambda)$ profile intercepted by the slice:

$$\lambda_{\rm shift} = \frac{\int_{-w/2}^{+w/2} \lambda \times \mathcal{F}(\lambda)\, {\rm d}\lambda}{\int_{-w/2}^{+w/2} \mathcal{F}(\lambda)\, {\rm d}\lambda} . \quad \text{(C2)}$$

where λ denotes the dispersion-axis coordinate across the projected slice width rather than the wavelength. This expression captures the fact that asymmetric illumination of the slice can bias the measured wavelength centroid. Following Y. Isobe et al. (2023a), and assuming that $\mathcal{F}(\lambda)$ can be locally approximated by a second-order polynomial ($\mathcal{F}(\lambda) \approx a\lambda^2 + b\lambda + c$), then equation (C2) can be simplified by performing the integration:

$$\lambda_{\rm shift} = w \times \frac{bw}{aw^2 + 12c} \quad \text{(C3)}$$

We then consider three adjacent IFU slices on the detector, at the dispersion axis coordinates $\lambda_{i-1} = -w$, $\lambda_i = 0$, and $\lambda_{i+1} = +w$, such that the central wavelength slice 'i' contains the peak of Hγ line emission. The fluxes measured in each of these slices are therefore:

$$\mathcal{F}_{i+1} \equiv \mathcal{F}(\lambda_{i+1}) = aw^2 + bw + c \quad \text{(C4)}$$
$$\mathcal{F}_{i-1} \equiv \mathcal{F}(\lambda_{i-1}) = aw^2 - bw + c \quad \text{(C5)}$$
$$\mathcal{F}_{i} \equiv \mathcal{F}(\lambda_{i}) = c \quad \text{(C6)}$$

Using these three parametrization equations for the fluxes observed on the three adjacent slices, we can further simplify equation (C3):

$$\lambda_{\rm shift} = w \times \frac{\mathcal{F}_{i+1} - \mathcal{F}_{i-1}}{\mathcal{F}_{i+1} + 22 \times \mathcal{F}_i + \mathcal{F}_{i-1}} , \quad \text{(C7)}$$

This formulation provides an estimate of the wavelength bias induced by slice-to-slice flux gradients. For *JWST*/NIRSpec, the undispersed IFU slices are 2 pixels wide according to *JWST* documentation.[6] Using the spectral dispersion and LSF appropriate for the observed Hγ wavelength, this corresponds to an effective projected width of $w \approx 35.8$ Å. The peak-to-peak amplitude of the rotational pattern resulting from our slit geometry model is ≈ 55 km s^{-1}, ~ 3.2 times smaller than in the observed data (≈ 175 km s^{-1}). However, if we compare the 5th – 95th percentiles amplitudes, the discrepancy is reduced (114 km s^{-1} in the observed data and 44 km s^{-1} in our simple model). We emphasize that our implementation represents a highly simplified, first-order description of the IFU slit geometry and does not capture more subtle instrumental effects or deviations of the slit geometry from a simple, parametric form. In conclusion, while instrumental systematics may plausibly account for a substantial fraction of the observed velocity gradient, we are not able to fully rule out the hypothesis that this kinematic pattern might be real, which could imply that the MACS0647-JD1 system would consist of two bright clumps within the same rotating disc.

APPENDIX D: PROSPECTOR SED FITS OF SPECTROSCOPY AND PHOTOMETRY

In Figs D1 and D2, we show our results from the PROSPECTOR fits based on the spectra and photometric fluxes corresponding to the apertures of the two stellar components (SE-C and NW-C in Fig. 2b). Our fitting method is described in Section 3.3.

[6] https://jwst-docs.stsci.edu/jwst-near-infrared-spectrograph/nirspec-observing-modes/nirspec-ifu-spectroscopy

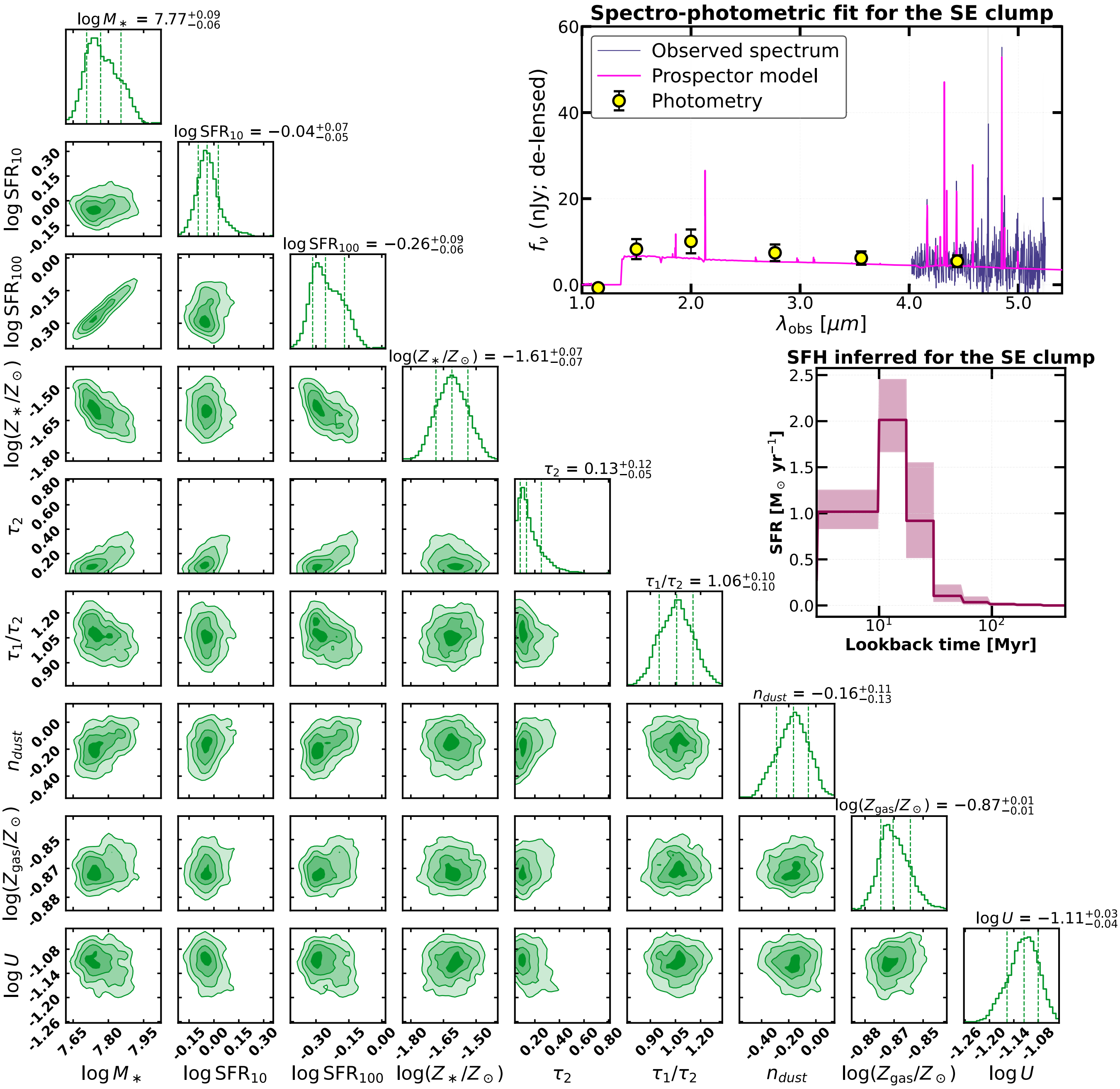

Figure D1. In this figure, we present the PROSPECTOR -fitting results for the more massive stellar component (the SE-C). The corner plot displays the marginalized 1D posterior distribution and the 2D correlations involving the following parameters: the logarithm of the stellar mass (in solar masses), the logarithms of SFR averaged over the 10 or 100 Myr prior to observation (in $M_{\odot}\,yr^{-1}$), stellar metallicity, the optical depth of the diffuse ISM (τ_2), the extra-additional factor of attenuation towards the birth clouds (τ_1/τ_2), the dust attenuation curve slope, $n_{\rm dust}$, the gas-phase metallicity, and the ionization parameter. The top-right inset panel shows the resulting SED model for the SE-C, while the central-right inset panel displays the SFH inferred by PROSPECTOR.

[1]*Kavli Institute for Cosmology, University of Cambridge, Madingley Road, Cambridge CB3 0HA, UK*
[2]*Cavendish Laboratory – Astrophysics Group, University of Cambridge, 19 JJ Thomson Avenue, Cambridge CB3 0HE, UK*
[3]*Department of Physics and Astronomy, University College London, Gower Street, London WC1E 6BT, UK*
[4]*Waseda Research Institute for Science and Engineering, Faculty of Science and Engineering, Waseda University, 3-4-1, Okubo, Shinjuku, Tokyo 169-8555, Japan*
[5]*Centro de Astrobiología (CAB), CSIC-INTA, Ctra. de Ajalvir km 4, Torrejón de Ardoz, E-28850, Madrid, Spain*
[6]*Sub-Department of Astrophysics, Department of Physics, University of Oxford, Denys Wilkinson Building, Keble Road, Oxford, OX1 3RH, UK*
[7]*Sorbonne Université, CNRS, UMR 7095, Institut d'Astrophysique de Paris, 98 bis bd Arago, F-75014 Paris, France*
[8]*Max-Planck-Institut für extraterrestrische Physik (MPE), Gießenbachstraße 1, D-85748 Garching, Germany*
[9]*INAF – Osservatorio Astrofisco di Arcetri, largo E. Fermi 5, I-50127 Firenze, Italy*

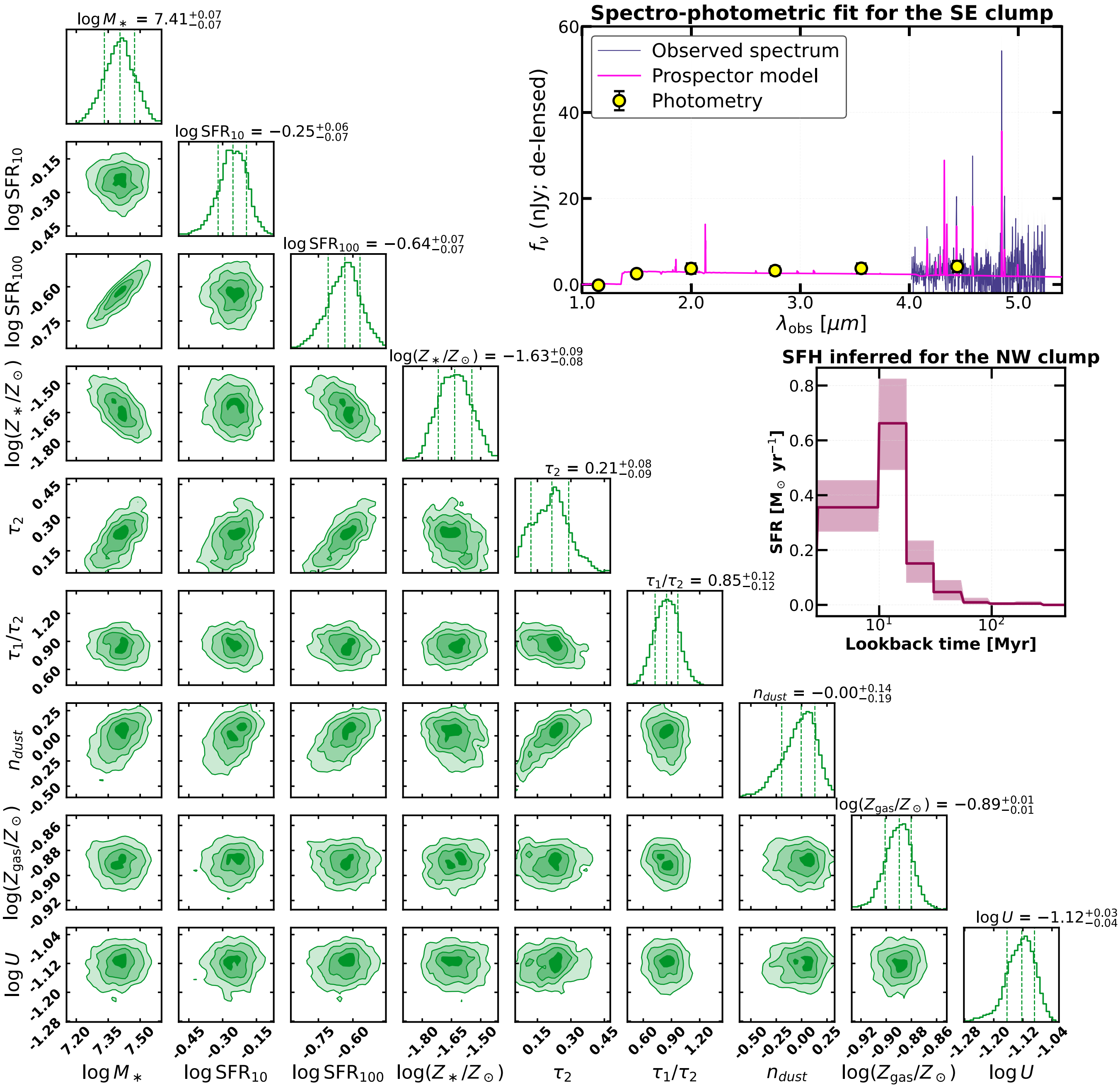

Figure D2. This figure is equivalent to Fig. D1, but it shows the PROSPECTOR best-fitting parameters in the case of the less massive stellar component (the NW-C). The top-right inset panel shows the SED model for the NW-C, while the central-right inset panel displays the SFH inferred by PROSPECTOR.

[10]*European Space Agency, c/o Space Telescope Science Institute, 3700 San Martin Drive, Baltimore MD 21218, USA*
[11]*Scuola Normale Superiore, Piazza dei Cavalieri 7, I-56126 Pisa, Italy*
[12]*Association of Universities for Research in Astronomy (AURA) Inc. for the European Space Agency (ESA), STScI, Baltimore, MD 21218, USA*
[13]*Center for Astrophysical Sciences, Department of Physics and Astronomy, The Johns Hopkins University, 3400 N Charles St. Baltimore, MD 21218, USA*
[14]*European Southern Observatory, Karl Schwarzschild Straße 2, D-85748 Garching bei München, Germany*
[15]*Department of Astronomy, University of Texas, Austin TX 78712, USA*
[16]*Dipartimento di Fisica e Astronomia, Università di Firenze, Via G. Sansone 1, I-50019, Sesto F.no (Firenze), Italy*
[17]*Cosmic Dawn Center (DAWN), Copenhagen, Denmark*
[18]*Niels Bohr Institute, University of Copenhagen, Jagtvej 128, DK-2200 Copenhagen, Denmark*

This paper has been typeset from a TEX/LATEX file prepared by the author.